

Angular correlation function of 1.5 million LRGs: clustering evolution and a search for BAO

U. Sawangwit^{1*}, T. Shanks¹, F. B. Abdalla², R. D. Cannon³, S. M. Croom⁴,
 A. C. Edge⁵, Nicholas P. Ross^{1,6} and D. A. Wake^{1,7}

¹Physics Department, University of Durham, South Road, Durham, DH1 3LE, UK

²Department of Physics and Astronomy, University College London, Gower Street, London, WC1E 6BT, UK

³Anglo-Australian Observatory, PO Box 296, Epping, NSW 1710, Australia

⁴School of Physics, University of Sydney, NSW 2006, Australia

⁵Institute for Computational Cosmology, University of Durham, South Road, Durham, DH1 3LE, UK

⁶Department of Astronomy and Astrophysics, The Pennsylvania State University, University Park, PA 16802, USA

⁷Department of Astronomy, Yale University, CT 06520, USA

5 December 2018

ABSTRACT

We present the angular correlation function measured from photometric samples comprising 1 562 800 luminous red galaxies (LRGs). Three LRG samples were extracted from the Sloan Digital Sky Survey (SDSS) imaging data, based on colour-cut selections at redshifts, $z \sim 0.35, 0.55$ and 0.7 as calibrated by the spectroscopic surveys, SDSS-LRG, 2dF-SDSS LRG and QSO (2SLAQ), and the AAOmega LRG survey. The galaxy samples cover $\sim 7600 \text{ deg}^2$ of sky, probing a total cosmic volume of $\sim 5.5 h^{-3} \text{ Gpc}^3$.

The small and intermediate scale correlation functions generally show significant deviations from a single power-law fit with a well-detected break at $\sim 1 h^{-1} \text{ Mpc}$, consistent with the transition scale between the 1– and 2– halo terms in halo occupation models. For galaxy separations $1 - 20 h^{-1} \text{ Mpc}$ and at fixed luminosity, we see virtually no evolution of the clustering with redshift and the data is consistent with a simple high peaks biasing model where the comoving LRG space density is constant with z . At fixed z , the LRG clustering amplitude increases with luminosity in accordance with the simple high peaks model, with a typical LRG dark matter halo mass $> 10^{13} h^{-1} M_\odot$. For $r < 1 h^{-1} \text{ Mpc}$, the evolution is faster and the clustering decreases towards high redshift consistent with a virialised clustering model. Again this result is consistent with a model where the LRG space density is constant with redshift.

At large scales, our highest S/N combined $w(\theta)$ result, in its raw form, shows an apparent peak in reasonable agreement with the acoustic peak detected by Eisenstein et al. (2005). However, this feature does not scale with depth in the expected manner. Furthermore, when corrections for possible systematics are taken into account the correlation function may not be consistent with as high amplitude a peak as claimed by Eisenstein et al. This conclusion is strongly supported by independent angular power-spectral analyses of similar LRG samples. The $w(\theta)$ shape may then still be consistent with what is expected from the linear structure growth of a scale-invariant spectrum of initial perturbations, perhaps including a lower amplitude acoustic peak.

Key words: galaxies: clustering – luminous red galaxies: general – cosmology: observations – large-scale structure of Universe.

1 INTRODUCTION

The galaxy two-point function whether in its correlation function or power spectrum form has long been recognised

as a powerful statistical tool for studying Large-Scale Structure (LSS) of the Universe (Peebles 1980). In an isotropic and homogeneous Universe, if the density fluctuation arises from a Gaussian random process, the two-point correlation function, $\xi(r)$, and its Fourier transform, $P(k)$, contains a complete description of such fluctuations. It has been used

* E-mail: utane.sawangwit@durham.ac.uk

to measure the clustering strength of galaxies in numerous galaxy surveys (see e.g. Groth & Peebles 1977; Shanks et al. 1989; Baugh & Efstathiou 1993; Ratcliffe et al. 1998) and the observed $\xi(r)$ is reasonably well represented by a power-law of the form $\xi(r) = (r/r_0)^{-1.8}$ over a large range of scales, $\sim 100 h^{-1} \text{ kpc} - 10 h^{-1} \text{ Mpc}$, where r_0 is approximately $5 h^{-1} \text{ Mpc}$.

More recently, large galaxy redshift surveys have become available (SDSS:York et al. 2000, 2dFGRS:Colless et al. 2001) and these surveys provide a perfect opportunity to exploit the two-point function as a tool to constrain cosmological parameters (Hawkins et al. 2003; Cole et al. 2005; Eisenstein et al. 2005; Tegmark et al. 2006; Percival et al. 2007) which in turn provides an excellent test for our current understanding of the Universe and the processes by which the LSS were formed.

In the past, when galaxy redshift surveys were less available, the angular correlation function, $w(\theta)$, was heavily utilised in the analysis of imaging galaxy samples. The spatial correlation function, $\xi(r)$, can be related to $w(\theta)$ via Limber's equation (Limber 1953), alternatively $w(\theta)$ can be inverted to $\xi(r)$ using Lucy's iterative technique (Lucy 1974), both approaches providing a means to recover the 3-D clustering information numerically. Even today, galaxy imaging surveys still tend to cover a bigger area of the sky and occupy a larger volume than redshift surveys and therefore could offer a route to a more accurate estimation of the correlation function and power spectrum (see e.g. Baugh & Efstathiou 1993).

As mentioned above, the correlation function at small to intermediate scales can be approximately described by a single power-law which also results in a power-law $w(\theta)$ but with a slope of $1 - \gamma$. However with larger sample sizes, recent analyses of galaxy distributions start to show a deviation from a simple power-law (Zehavi et al. 2005b; Phleps et al. 2006; Ross et al. 2007; Blake et al. 2008, see also Shanks et al. 1983). This poses a challenge for a physical explanation and understanding of non-linear evolution of structure formation. Several authors attempted to fit such correlation function using a description of halo model framework (e.g. Cooray & Sheth 2002) invoking a transition between 1- and 2- halo terms which occurs at $\sim 1 h^{-1} \text{ Mpc}$ where the feature is observed. This distance scale could potentially be used as a 'standard ruler' in tracking the expansion history of the Universe, provided that its physical origin is well understood and the scale can be accurately calibrated.

Another feature in the correlation function predicted by the standard ΛCDM model is the 'Baryon Acoustic Oscillations' (BAO). BAO arise from sound waves that propagated in the hot plasma of tightly coupled photons and baryons in the early Universe. As the Universe expands and temperature drops below 3000 K, photons decouple from the baryons at the so called 'epoch of recombination'. The sound speed drops dramatically and oscillatory pattern imprinted on the baryon distribution as well as the temperature distribution of the photons which approximately 13 billions years after the Big Bang revealed as the acoustic oscillations in the temperature anisotropies of the CMB. The equivalent but attenuated feature exists in the clustering of matter, as baryons fall into dark matter potential wells after the recombination. In recent years, the

acoustic peak scale in the LSS has been proposed as a potential 'standard ruler' (e.g. Blake & Glazebrook 2003; Glazebrook et al. 2007; McDonald & Eisenstein 2007) for constraining the Dark Energy equation of state ($w = p/\rho c^2$) and its evolution.

For the BAO approach to the study of Dark Energy to yield a competitive result, a large survey of several million galaxies is generally required (Blake & Glazebrook 2003; Seo & Eisenstein 2003; Parkinson et al. 2007; Angulo et al. 2008). A galaxy spectroscopic redshift survey would require a substantial amount of time and resources. An alternative route which will enable a quicker and larger area covered is through the use photometric redshift (photo-z hereafter) at the expense of the ability to probe the radial component directly. The photo-z errors are usually worse than spectroscopic redshift errors, but this can be compensated by a larger survey and deeper imaging.

The potential of the distribution of Luminous Red Galaxies (LRGs) as a powerful cosmological probe has long been appreciated (Gladders & Yee 2000; Eisenstein et al. 2001). Their intrinsically high luminosities provide us with at least two advantages, one being the ability to observe such a population out to a greater distance whilst the other is the possibility of detecting the small overdensity of the BAO in matter distribution at $\sim 100 h^{-1} \text{ Mpc}$ owing to their high linear bias¹. In addition, their typically uniform Spectral Energy Distributions (SEDs) allow a homogeneous sample to be selected over the volume of interest. Moreover, the strong 4000 Å break in their SEDs make them an ideal candidate for the photometric redshift route or even a colour-magnitude cut as demonstrated by the success of the target selection algorithm of three LRG spectroscopic follow-ups using SDSS imaging. In fact, the first clear detection of the BAO in the galaxy distribution came from the analysis of LRG clustering at low redshift (Eisenstein et al. 2005).

Here we shall present new measurements of the angular correlation functions determined from colour selected LRG samples. We shall show that this route provides redshift distribution, $n(z)$, widths that are close to the current photo-z accuracy, with none of the associated systematic problems. Indeed, one of our aims is to assess the efficiency of this route to BAO measurement compared to a full 3-D redshift correlation function. This possibility arises because the $n(z)$ width that we obtain is comparable to the $\approx 100 h^{-1} \text{ Mpc}$ scale of the expected acoustic peak. It is important therefore to assess how much this 'colour-cut' route can compete with spectroscopic redshifts and indeed photometric redshifts in terms of the BAO detection efficiency.

A similar clustering analysis measuring $w(\theta)$ of LRGs with photo-z's has been carried out by Blake et al. (2008). Equipped with a higher-redshift LRG selection algorithm whose effectiveness has been tested with the new LRG spectroscopic redshift survey, VST-AAΩ *ATLAS* pilot run (Ross et al. 2008), our approach is an improvement over Blake et al. (2008) as it probes an almost four times larger

¹ This is the well known luminosity dependant bias as shown observationally by e.g. Norberg et al. (2002); Zehavi et al. (2005b) and is expected in hierarchical clustering cold dark matter universe (Benson et al. 2001).

Table 1. Summary of the properties of LRG samples used in this study.

Sample	\bar{z}	Number	Density (deg $^{-2}$)	Magnitude (AB)
SDSS	0.35	106 699	~13	$17.5 \leq r_{\text{petro}} < 19.5$
2SLAQ	0.55	655 775	~85	$17.5 < i_{\text{deV}} < 19.8$
AAΩ	0.68	800 346	~105	$19.8 < i_{\text{deV}} \leq 20.5$

cosmic volume and we extend the analysis to large scales to search for the BAO peak.

The layout of this paper is as follows. An overview of the galaxy samples used here is given in §2. §3 describes the techniques for estimating the angular correlation functions and their statistical uncertainties. We then present the correlation results in §4. In §5, the clustering evolution and the typical dark matter halo masses of these LRGs are discussed. We then investigate a possibility of the acoustic peak detection in the $w(\theta)$ from the combined sample and in the future wide-field photo-z LRG surveys in §6. Finally, summary and conclusions of our study are presented in §7.

2 DATA

The galaxy samples used in this study were selected photometrically from SDSS DR5 (Adelman-McCarthy et al. 2007) imaging data based on three LRG spectroscopic redshift surveys with $\bar{z} \sim 0.35, 0.55$ and 0.7 (Eisenstein et al. 2001; Cannon et al. 2006; Ross et al. 2008). In summary, these surveys utilised a crude but effective determination of photometric redshift as the strong 4000 Å feature of a typical LRG spectral energy distribution (SED) moves through SDSS u, g, r, i , and z bandpasses (Fukugita et al. 1996; Smith et al. 2002). In each survey, a two-colour system (either $g - r$ versus $r - i$ or $r - i$ versus $i - z$) suitable for the desired redshift range was used in conjunction with r or i -band magnitude to select luminous intrinsically red galaxies. The method employed by these surveys has been proven to be highly effective in selecting LRGs in the target redshift range. The full selection criteria will not be repeated here but a summary of the algorithms and any additional criteria will be highlighted below (see Eisenstein et al. 2001; Cannon et al. 2006; Ross et al. 2008 for further details). Redshift distributions, $n(z)$, of the LRGs from the spectroscopic surveys utilised in this work are shown in Fig. 1. The LRG samples corresponding to the above $n(z)$ have been carefully selected to match our selection criteria hence these $n(z)$ will be assumed in determining the 3-D correlation functions, $\xi(r)$, from their projected counterparts, $w(\theta)$, via the Limber (1953) equation.

All magnitudes and colours are given in SDSS AB system and are corrected for extinction using the Galactic dust map of Schlegel, Finkbeiner & Davis (1998). In this analysis, we only used the galaxy samples in the most contiguous part of the survey, i.e. the northern Galactic cap (NGC). All colours described below refer to the differences in ‘model’ magnitudes (see Lupton et al. 2001, for a review on model magnitudes) unless otherwise stated.

Hereafter we shall refer to the photometrically selected sample (not to be confused with the spectroscopic sample

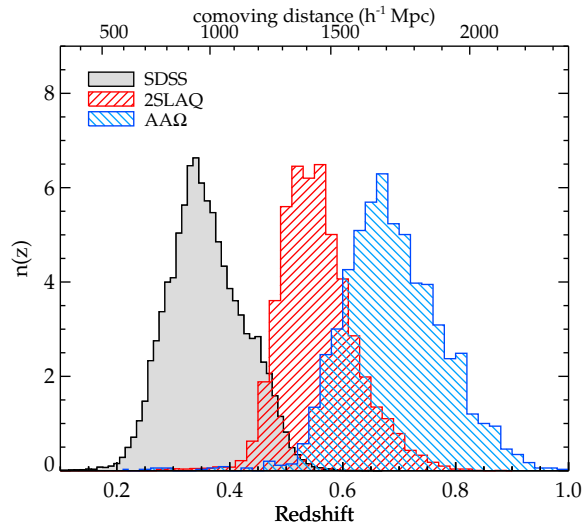


Figure 1. Normalised redshift distributions, $n(z)$, of the three LRG spectroscopic surveys used as the basis for selection criteria in this study.

from which they are associated) at average redshift of 0.35 , 0.55 and 0.7 as the ‘SDSS LRG’, ‘2SLAQ LRG’ and ‘AAΩ LRG’, respectively.

2.1 SDSS LRG

The sample used here is similar to the target sample of the recently completed SDSS-LRG spectroscopic survey which contains $\approx 100 000$ spectra and cover over $1 h^{-3} \text{ Gpc}^3$. These objects are classified as LRGs on the basis of their colours and magnitudes following Eisenstein et al. (2001, E01 hereafter). The sample is approximately volume-limited up to $z \sim 0.38$ and spans out to $z \sim 0.5$. The selection is done using $(g - r)$ and $(r - i)$ colours coupled with r -band Petrosian (1976) magnitude system. The algorithm is designed to extract LRGs in two different (but slightly overlapped) regions of the gri colour space and hence using two selection criteria (*Cut I* and *Cut II* in E01) as naturally suggested by the locus of early-type galaxy on this colour plane (see Fig. 2). The tracks shown in Fig. 2 were constructed using a spectral evolution model of stellar populations (Bruzual & Charlot 2003) with output spectra mimicking a typical SED of the LRGs. The stellar populations were formed at $z \sim 10$ and then evolve with two different scenarios, namely a) passive evolution of an instantaneous star formation (single burst), and b) exponentially decayed star formation rate (SFR) with e -folding time of 1 Gyr. Solar metallicity and Salpeter (1955) Initial Mass Function (IMF) were assumed in both evolutionary models.

We used the same colour-magnitude selection as that described by E01 but with additional restriction on the r -band apparent magnitudes of the objects, i.e. $r_{\text{petro}} \geq 17.5$. This is due mainly to two reasons, a) to separate out the objects with $z < 0.2$ because *Cut I* is too permissive and allows under-luminous objects to enter the sample below redshift 0.2 as also emphasised by E01, and b) to tighten the redshift distribution of our sample while maintaining the number of objects and its average redshift (see Fig. 3).

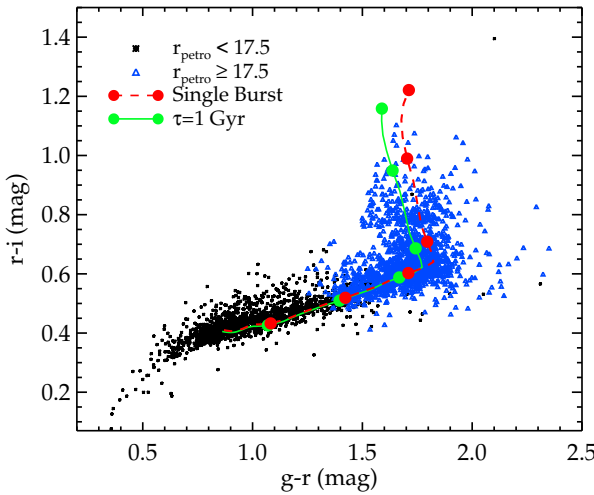


Figure 2. The colour-colour plot of SDSS LRG *cut I* and *II* showing their positions on the gri colour plane compared to the predicted colour-colour locus (observer frame) of typical early-type galaxies as a function of redshift (see text for more details). Each solid circle denotes the redshift evolution of the colour-colour tracks at the interval of 0.1 beginning with $z = 0.1$ (bottom left).

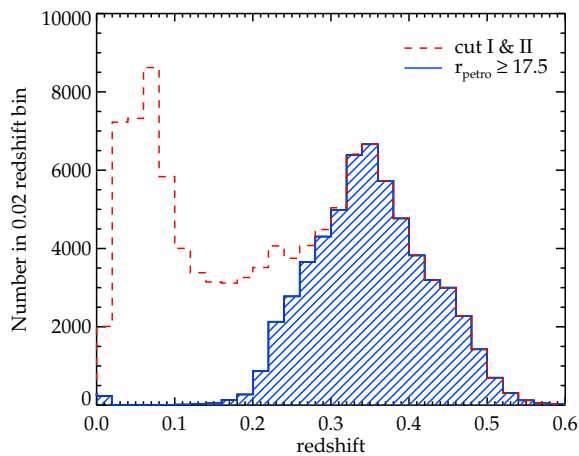


Figure 3. The number of objects as a function of redshift from SDSS LRG spectroscopic redshift survey also shown is the subset of *Cut I* and *II* with additional magnitude cut, $r_{\text{petro}} \geq 17.5$, applied.

The selection criteria mentioned above also has another star-galaxy separation algorithm apart from the pipeline PHOTO classification (Lupton et al. 2001). This was done by setting a lower limit on the differences in r -band point-spread function (PSF) magnitudes and model magnitudes as most galaxies populate the upper part of $r_{\text{PSF}} - r_{\text{model}}$ space compare to the foreground star of similar apparent magnitude. The algorithm has been proven to be quite effective (less than 1 per cent stellar contamination) for this range of redshift and magnitude although *Cut II* needs a more restrictive threshold, $r_{\text{PSF}} - r_{\text{model}} > 0.5$ as compared to 0.3 for *Cut I*.

In practice, the LRG sample described here can be extracted from the SDSS DR5 imaging database using the SQL query by setting the flag `PRIMTARGET` to `GALAXY_RED`. This yields a catalogue of approximately 200 000 objects which after applying the additional magnitude cut mentioned above, becomes 106 699 objects and results in the sky surface density of about 13 objects per square degree.

2.2 2SLAQ LRG

The 2dF-SDSS LRG and Quasar Survey (2SLAQ) is the spectroscopic follow-up of intermediate to high redshift ($z > 0.4$) LRGs from photometric data of SDSS DR4 (Adelman-McCarthy et al. 2006) using the two-degree Field (2dF) instrument on the Anglo-Australian Telescope (AAT). This survey is now completed and contains approximately 13 000 *bona fide* LRGs with over 90 per cent have $0.45 < z < 0.8$ in two narrow equatorial strips covering 180 square degrees. The primary sample of the survey (*Sample 8*, Cannon et al. 2006; C06 hereafter) was selected using $(g - r)$ versus $(r - i)$ colours and ‘de Vaucouleurs’ i -band magnitude ($17.5 < i_{\text{dev}} < 19.8$). The colour selection of *Sample 8* is similar to that of *Cut II* which utilises the upturn of the early-type galaxy locus in gri colour plane and hence is immune against the confusion with the late-type galaxy locus at higher redshift (see Fig. 2 in E01) but the scattering up in colour of interlopers from lower redshift and contamination of M-stars can also affect the accuracy of the selection. The latter could be prevented by using a similar method for star-galaxy separation as described in the last section but in this case we used the i -band magnitude rather than the r -band. Following C06, two criteria were used,

$$i_{\text{psf}} - i_{\text{model}} > 0.2(21 - i_{\text{dev}}) \quad (1)$$

and

$$\text{radius}_{\text{dev}(i)} > 0.2, \quad (2)$$

where $\text{radius}_{\text{dev}(i)}$ is de Vaucouleurs radius fit of the i -band photometry. As reported by C06, approximately 5 per cent of the cool dwarf M-star is still present in their sample and we shall assume this value when correcting for the dilution of the correlation signal due to the uncorrelated nature of foreground stars and the LRGs. In this work, we only use *Sample 8* as this provides us with a narrower $n(z)$ and higher average redshift than the whole 2SLAQ sample.

A sample of 655 775 photometrically selected LRG candidates (~ 5 per cent stellar contamination) is returned by the SDSS DR5 ‘Best Imaging’ database when the *Sample 8* selection criteria is used in the SQL query from table `GALAXY`. Objects with `BRIGHT` or `SATURATED` or `BLENDED` but not `DEBLENDED` flags are not included in our sample.

2.3 AAΩ LRG

The AAΩ-AAT LRG Pilot observing run was carried out in March 2006 by Ross et al. (2008, and reference therein) as a ‘Proof of Concept’ for a large spectroscopic redshift survey, VST-AAΩ *ATLAS* (Shanks et al. 2007), using the new AAΩ instrument on the AAT. The survey was designed

to target photometrically selected LRGs out to $z \sim 1.0$ with the average redshift of 0.7. The target sample was observed in three 2-degree fields including the COSMOS field (Scoville et al. 2007), the COMBO-17 S11 field (Wolf et al. 2001), and 2SLAQ d05 field (Cannon et al. 2006).

We follow the survey main selection criteria, $19.8 < i_{\text{dev}} \leq 20.5$ together with the riz colour cuts as described by Ross et al. (2008). In summary, the cut utilises the upturn of the early-type galaxy colour-colour locus similar to that used by 2SLAQ and SDSS LRG surveys. The turning point of the track on the riz colour plane occurs at $z = 0.6 - 0.7$ as the 4000 Å feature moves from the SDSS r to i band whilst this happens at $z \sim 0.4$ in the gri case. The selection technique has been proven to work reasonably well by the observed redshift distribution. This is further confirmed by the ongoing AAT-AAΩ LRG project, the down-sized version of the VST-AAΩ *ATLAS* survey, designed to observed several thousands of LRG redshifts for photo-z calibration and a clustering evolution study. The $n(z)$ (Fig. 1) used in inferring the 3-D clustering information also includes ~ 2000 AAΩ LRG redshifts taken during the run in June 2008 (Sawangwit et al. 2009, in prep.).

As emphasised by Ross et al. (2008), the stellar contamination in the sample can be readily reduced to ≈ 16 per cent by imposing star-galaxy separation in the z -band without any significant loss of the genuine galaxies. Although the level of contamination could be further reduced by using near-infrared photometry, we do not attempt it here as there is no infrared survey that covers the entire SDSS DR5 NGC sky with similar depth. Therefore we shall use the quoted contamination fraction when correcting the measured $w(\theta)$ for the same reason mentioned in §2.2. Since no expression for star-galaxy separation is given in Ross et al. (2008), here such a procedure is performed using an equation defining the dashed line in their Fig. 3,

$$z_{\text{psf}} - z_{\text{model}} > 0.53 + 0.53(19.0 - z_{\text{model}}) \quad (3)$$

Applying the above selection rules on the ‘Best Imaging’ data of the SDSS DR5 yields a photometric sample of 800 346 high-redshift LRG candidates with the sky surface density of approximately 110 objects per square degree. As with the 2SLAQ LRG sample, objects with BRIGHT or SATURATED or BLENDED but not DEBLENDED flags are discarded from our sample.

3 ESTIMATING $w(\theta)$ AND ITS ERROR

3.1 Optimal estimator and techniques

The two-point correlation function, $\xi(r)$, measures the excess probability of finding a pair of objects separated by distance r relative to that expected from a randomly distributed process. The joint probability of finding two objects of interest (in this case the LRGs) in the volume elements δV_1 and δV_2 separated by a distance r is given by

$$\delta P(r) = n^2 [1 + \xi(r)] \delta V_1 \delta V_2 \quad (4)$$

where n is the number space density of the sample. In practice, redshift of individual object is required to estimate the separation between a given pair. However if such redshift information is not available as in this study, the sky projected

version, $w(\theta)$, can be used to analyse the clustering property of the sample instead. The 2D equivalent of Eq. 4 is

$$\delta P(\theta) = \aleph^2 [1 + w(\theta)] \delta \Omega_1 \delta \Omega_2 \quad (5)$$

where \aleph is the surface density of the objects and $\delta P(\theta)$ is now the joint probability of finding two objects in solid angle $\delta \Omega_1$ and $\delta \Omega_2$ separated by angle θ .

Two possible routes for estimating $w(\theta)$ are the pixelisation of galaxy number overdensity, $\delta_g = \delta_n / \bar{n}$ and pair counting. The pixelisation approach usually requires less computation time but its smallest scale probed is limited by the pixel size. We choose to follow the latter. To calculate $w(\theta)$ using the pair counting method, one usually generate a random catalogue whose angular selection function is described by the survey. The number of random points are generally required to be 10 times the number of objects or more. This is necessary to reduce the shot noise. Our random catalogue for each sample has ~ 20 times the number of LRGs in SDSS and 10 times for 2SLAQ and AAΩ-pilot (see next section for details on how this was achieved).

We compute $w(\theta)$ using the minimum variance estimator of Landy & Szalay (1993). It is also an unbiased estimator (Martínez & Saar 2002) for 2PCF as it can be reduced to the exact theoretical definition of 2PCF, i.e a variance of density fluctuation in Gaussian field, $\xi(r) = \langle \delta(\mathbf{x}) \delta(\mathbf{x} + \mathbf{r}) \rangle$. The form of this estimator is

$$w_{\text{LS}}(\theta) = 1 + \left(\frac{N_{rd}}{N} \right)^2 \frac{DD(\theta)}{RR(\theta)} - 2 \left(\frac{N_{rd}}{N} \right) \frac{DR(\theta)}{RR(\theta)} \quad (6)$$

where $DD(\theta)$ is the number of LRG-LRG pairs with angular separation within the angular bin centres at θ . $DR(\theta)$ and $RR(\theta)$ are the numbers of LRG-random and random-random pairs, respectively. N_{rd}/N ratio is required for normalisation. N_{rd} is the total number of random points and N is the total number of LRGs. We use a logarithmic bin width of $\Delta \log(\theta/\text{arcmin}) = 0.176$ for $\theta = 0.1'$ to $50'$ and a linear bin width of $20'$ at scales larger than $50'$.

The uncertainty in the number density of the sample could lead to a bias in the estimation of $w(\theta)$ when using Landy-Szalay estimator especially at large scale where the amplitude is small and hence we also utilise the Hamilton (1993) estimator, given by

$$w_{\text{HM}}(\theta) = \frac{DD(\theta) \cdot RR(\theta)}{DR(\theta)^2} - 1 \quad (7)$$

which requires no normalisation. We used the Hamilton estimator to cross-check our w_{LS} for each sample and found the difference given by the two estimators to be negligible in all three samples.

For the purpose of determining statistical uncertainty in our measurement, three methods of estimating the errors are considered. The first method is the simple Poisson error given by

$$\sigma_{\text{Poi}}(\theta) = \frac{1 + w(\theta)}{\sqrt{DD(\theta)}} \quad (8)$$

For the second method, *field-to-field* error, we split the sample into 24 subfields of approximately equal size. These subfields are large enough for estimating the correlation function up to the scale of interest. This is simply a standard deviation of the measurement in each subfield from the best estimate and is calculated using

$$\sigma_{\text{FtF}}^2(\theta) = \frac{1}{N-1} \sum_{i=1}^N \frac{DR_i(\theta)}{DR(\theta)} [w_i(\theta) - w(\theta)]^2 \quad (9)$$

where N is the total number of subfields, $w_i(\theta)$ is a measurement from the i th subfield and $w(\theta)$ is measured using the whole sample. The deviation of the angular correlation function computed in each subfield is weighted by $DR_i(\theta)/DR(\theta)$ to account for their relative sizes.

The third method is the *jackknife* resampling. This is a method of preference in a number of correlation studies (see e.g. Scranton et al. 2002; Zehavi et al. 2005a; Ross et al. 2007). The jackknife errors is computed using the deviation of $w(\theta)$ measured from the combined 23 subfields out of the 24 subfields. The subfields are the same as used for the estimation of *field-to-field* error above. $w(\theta)$ is calculated repeatedly, each time leaving out a different subfield and hence results in a total of 24 measurements. The jackknife error is then

$$\sigma_{\text{JK}}^2(\theta) = \sum_{i'=1}^N \frac{DR_{i'}(\theta)}{DR(\theta)} [w_{i'}(\theta) - w(\theta)]^2 \quad (10)$$

where $w_{i'}(\theta)$ is now an angular correlation function estimated using the whole sample except the i th subfield and $DR_{i'}(\theta)/DR(\theta)$ is approximately 23/24 with slight variation depending on the size of resampling field.

It is well known that the correlation function bins are correlated which could affect the confidence limit on the parameter estimation performed under the assumption that each data point is independent. Comparison of the estimated error using the field-to-field and jackknife techniques to the simple Poisson error can give a rough estimate of the deviation from the independent point assumption. This is plotted in Fig. 4 which shows that the assumption is valid on small scales where Poisson error is a fair estimate of the statistical uncertainty. However the same cannot be said on large scales where the data points are correlated and the independent point assumption no longer holds. At these scales, such statistical uncertainty is likely to be dominated by edge-effects and cosmic variance.

Fig. 4 also shows that the errors estimated using field-to-field and jackknife method are in good agreement at all angular scales except for 2SLAQ and AAΩ samples where the jackknife errors are slightly smaller towards the large scales but still agree within 10 per cent. The errors quoted in later sections are estimated using the jackknife resampling method.

The covariance matrix allows the correlation between each bin to be quantified and can be used in the fitting procedure to de-correlate the separation bins. We calculate the covariance matrix from the jackknife resampling using

$$\mathbf{C}_{ij} = (N-1) \langle [w(\theta_i) - \bar{w}(\theta_i)] \cdot [w(\theta_j) - \bar{w}(\theta_j)] \rangle \quad (11)$$

where $\bar{w}(\theta_j)$ is the mean angular correlation function of all the jackknife subsamples in the j th bin. Note that the difference between $w(\theta_j)$ and $w(\theta)$ estimated using the whole sample is negligible. We then proceed to compute the ‘correlation coefficient’, \mathbf{r}_{ij} , defined by

$$\mathbf{r}_{ij} = \frac{\mathbf{C}_{ij}}{\sqrt{\mathbf{C}_{ii} \cdot \mathbf{C}_{jj}}} \quad (12)$$

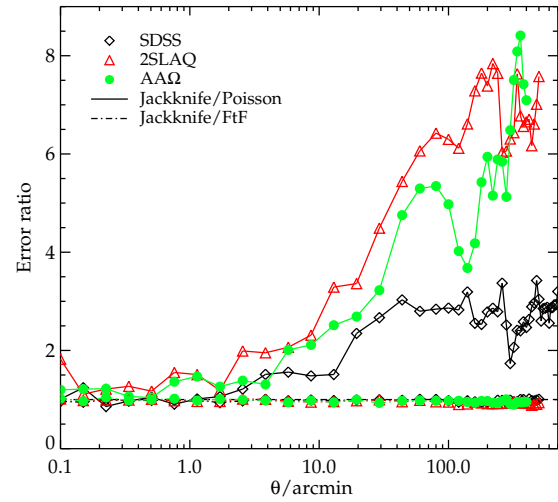


Figure 4. The ratio of jackknife to Poisson and field-to-field errors on the measurements of $w(\theta)$. The open diamonds, triangles and solid circles give the error ratios of $w(\theta)$ estimated from SDSS, 2SLAQ, and AAΩ LRG, respectively.

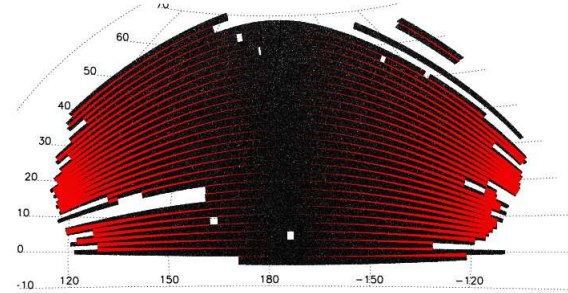


Figure 6. An equal area Aitoff projection of a random catalogue described in §3.2. The red/grey highlighted regions indicate the areas where adjacent stripes are overlapped. Note that the shading is purely diagrammatic to show the overlap regions and is unrelated to galaxy density.

Fig. 5 shows the correlation coefficients for the three samples which are strongly correlated at the largest scale considered and less at small scales confirming the simple correlation test using Poisson errors.

We use the *kd-trees* code (Moore et al. 2001) to minimise the computation time required in the pair counting procedure. The angular correlation function is estimated using the method described above and then correct for stellar contamination which reduce the amplitude by a factor $(1-f)^2$, where f is the contamination fraction for each sample given in §2.

3.2 Constructing random catalogues

In order to calculate the angular correlation function accurately, a random catalogue is required. This catalogue consists of randomly distributed points with the total number at least 10 times that of the data. Each random point is assigned a position in Right Ascension (RA) and Declination

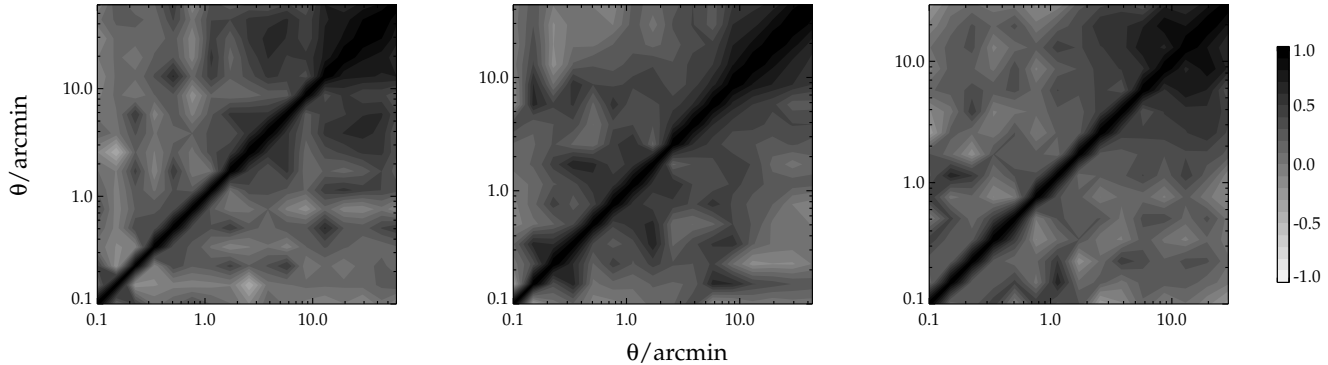


Figure 5. The correlation coefficients, r_{ij} , showing the level of correlation between each angular separation bin for SDSS, 2SLAQ, and AAΩ LRG (left to right). Note that for each sample we only show r_{ij} up to the angular separation corresponds to $\approx 20 h^{-1}$ Mpc where later we shall attempt to fit power-law forms to the measured $w(\theta)$'s.

(DEC). Since our sample spans a wide range in DEC (see Fig. 6 for the SDSS DR5 sky coverage), care must be taken to keep the surface number density constant assuming the survey completeness is constant and uniform throughout. Only the random points that satisfy the angular selection function of the survey as defined by the mask are selected.

The mask is constructed from ‘BEST’ DR5 imaging sky coverage given² in the survey coordinate (λ, η) and stripe number. The sky is drift scanned in a strip parallel to η and two strips are required to fill a stripe (York et al. 2000). Each stripe is 2.5° wide and their centres are separated by 2.5° . Further away from the survey equator ($RA_{2000} = 185^\circ$), the adjacent stripes become overlapped which account for almost 20 per cent of the sky coverage. The ‘BEST’ imaging database only keep the best photometry of the objects which have been detected more than once in the overlap regions.

At the faint magnitude limit of our sample, this could lead to a higher completeness in the overlap region and introduces bias in the estimated correlation function. This issue has also been addressed by Blake et al. (2007). They compared the measurement from the sample which omits the overlap region against their best estimate and found no significant difference. We follow their approach by excluding the overlap regions and re-calculating the angular correlation function of our faintest apparent magnitude sample, AAΩ-LRG, where the issue is expected to be the most severe. We found no significant change compared to our best estimate using the whole sample.

3.3 Inferring 3-D clustering

The angular correlation function estimated from the same population with the same clustering strength will have a different amplitude at a given angular scale if they are at different depths (redshifts) or have different redshift selection functions, $\phi(z)$. Therefore in order to accurately compare the clustering strengths of different samples inferred from $w(\theta)$, one needs to know the sample $\phi(z)$. Even if the redshifts of individual galaxies are not available, their 3-D

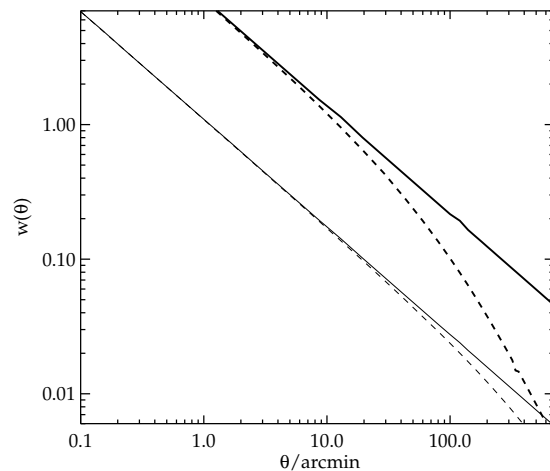


Figure 7. The angular correlation function computed using the full (dashed-lines) and approximate (solid-lines) Limber equation, derived using a power-law, $\xi(r) = (r/r_0)^{-\gamma}$ where $r_0 = 10 h^{-1}$ Mpc and $\gamma = 1.8$ with the SDSS LRG $n(z)$ for the thin lines and much narrower $n(z)$ (± 0.01 centred at $z = 0.35$) for the thick lines.

clustering information can be recovered if the sample redshift distribution, $n(z)$, is known. The equation that relates the spatial coherence length, r_0 , to the amplitude of $w(\theta)$ is usually referred to as Limber’s equation.

Recently, the accuracy of Limber’s equation has been called into question. This is due to the assumption made for Limber’s approximation that the selection function, $\phi(z)$, varies much more slowly than $\xi(r)$ in addition to the flat-sky (small angle) approximation. It was shown by Simon (2007) that such an assumption would lead to $w(\theta)$ being overestimated at large angle where the breakdown scale becomes smaller for narrower $\phi(z)$ (see Fig. 7). Here, we shall use the relativistic generalisation of Limber’s equation suggested by Phillipps et al. (1978) but without the approximation mentioned above. Following Phillipps et al. (1978) for the comoving case,

² <http://www.sdss.org/dr5>

$$w(\theta) = \frac{\int_0^\infty dz_1 f(z_1) \int_0^\infty dz_2 f(z_2) \xi(r)}{\left[\int_0^\infty dz f(z) \right]^2} \quad (13)$$

The source's radial distribution, $f(z)$, is simply given by the galaxy selection function, $\phi(z)$, as

$$f(z) \equiv \chi^2(z) \frac{d\chi(z)}{dz} n_c(z) \phi(z) \quad (14)$$

where χ is the radial comoving distance, $n_c(z)$ is the comoving number density of the sources and $r = r(\theta, z_1, z_2)$ is a comoving separation of the galaxy pair. We shall assume a spatially flat cosmology (see §4.2) hence

$$r \equiv \sqrt{\chi^2(z_1) + \chi^2(z_2) - 2\chi(z_1)\chi(z_2) \cos \theta} \quad (15)$$

Note that Eq. 13 can also be used to relate a non-power-law spatial correlation function to $w(\theta)$ unlike the conventional power-law approximation of Limber's equation (Phillipps et al. 1978).

Fig. 7 shows $w(\theta)$ computed using Eq. 13 (dashed lines) compared to the conventional Limber's approximation (solid lines) for a power-law $\xi(r)$ with clustering length $10 h^{-1}$ Mpc and $\gamma = 1.8$. The effect of a much narrower redshift distribution (thick lines) is also shown where the break scale becomes smaller and the power-law slope of $w(\theta)$ asymptotically approaches that of $\xi(r)$, agreeing with the finding of Simon (2007). We shall use Eq. 13 together with the known $n(z)$ to infer the 3-D spatial clustering of the LRGs.

4 RESULTS

4.1 Small and Intermediate Scales

We first look at the angular correlation function measured from the LRG sample at scales less than $\sim 1^\circ$ corresponding to approximately $20 h^{-1}$ Mpc where previous studies suggested that the spatial 2PCF can be described by a single power-law of the form $\xi(r) = (r/r_0)^{-\gamma}$ (typically $\gamma = 1.8$) and a single power-law $w(\theta)$ with slope $1 - \gamma$ is expected (see Fig. 7). However in this study, we find a deviation from a single power-law with a break in the slope at $\sim 1 h^{-1}$ Mpc in all three samples (less significant for the SDSS LRG). The measurement has a steeper slope at small scales ($< 1 h^{-1}$ Mpc) and is slightly flatter on scales up to $\sim 20 h^{-1}$ Mpc where it begins to drop sharply (see Fig. 8 and Fig. 9). The inflexion feature at $1 h^{-1}$ Mpc has also been reported in the spatial and semi-projected, $w_p(\sigma)$, correlation function by Zehavi et al. (2005a), Ross et al. (2007), Phleps et al. (2006), Blake et al. (2008) and detections go back as far as Shanks et al. (1983).

If we first consider $w(\theta)$ at scales smaller and larger than the break point separately, each can be roughly described by a power-law with a slope of ~ -1.15 ($\gamma = 2.15$), and ~ -0.83 ($\gamma = 1.83$), respectively. A more detailed analysis is performed by fitting a set of models to the measured $w(\theta)$ using a chi-squared minimisation method with the covariance matrix constructed from the jackknife resampling (see §3.1). Although several authors have attempted to fit the observed correlation function with that derived using the Halo model framework, here we only consider a set of simple power-law models. This allows us to quantify the significance of the deviation from the single power-law by com-

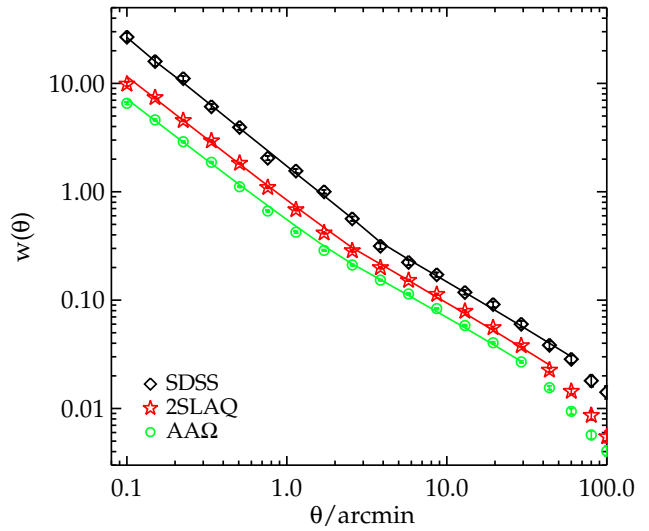


Figure 8. The angular correlation function measured from the three LRG samples. The solid lines are the projection of best-fit double power-law $\xi(r)$ with r_0 and γ given in Table 2 for each sample. The break scales occur at approximately a few arcminutes depending on the average redshift of the sample. This corresponds to a comoving separation of $\approx 1 h^{-1}$ Mpc (see Fig. 9).

paring its *goodness of fit* to a double power-law. We proceed by calculating

$$\chi^2 = \sum_{i,j=1}^N \Delta w(\theta_i) \mathbf{C}_{ij}^{-1} \Delta w(\theta_j) \quad (16)$$

where N is the number of angular bins, $\Delta w(\theta_i)$ is the difference between the measured angular correlation function and the model for the i th bin, and \mathbf{C}_{ij}^{-1} is the inverse of covariance matrix.

The single power-law fit is of the form $w(\theta) = (\theta/\theta_0)^{(1-\gamma)}$. We also recover the spatial clustering length, r_0 , and its slope through the fitting via Eq. 13. For a double power-law, the fitting procedure is performed separately at the scales smaller and larger than θ_b , corresponding to $\sim 1 h^{-1}$ Mpc for all three samples (see Fig. 9). The largest scale considered in the fitting for all cases is $\sim 20 h^{-1}$ Mpc where a steeper drop-off of $w(\theta)$ is observed.

In Fig. 9, the best-fit power-laws for all three samples are shown. The summary of the best-fit parameters are given in Table 2. Eq. 13 and 16 are then used to find the spatial clustering lengths and slopes that best describe our $w(\theta)$ results. The best-fit clustering slopes from r_0 - γ analysis using Limber's equation are in good agreement with that from θ_0 - γ and hence we only give the latter in Table 2. The clustering length (single power-law), r_0 , ranges from 7.5 to $8.7 h^{-1}$ Mpc, consistent with highly biased luminous galaxies. Single power-law fits to the data can be rejected in favour of the double power-law at the confidence level of 1.5σ for the SDSS LRG sample and more than 4σ for 2SLAQ and AAΩ LRG samples.

The best-fit slopes for all three samples at the same scales are in good agreement within the 1σ error. The SDSS LRG sample is more strongly clustered than the rest as ex-

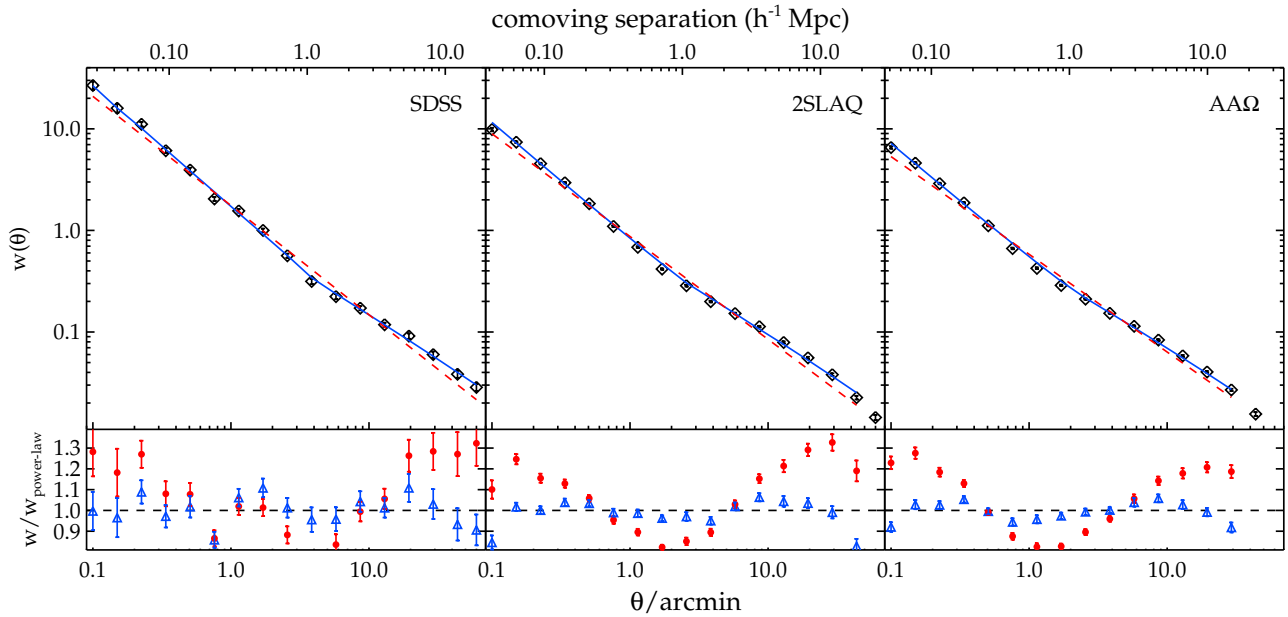


Figure 9. The angular correlation function with the best-fit single (red dashed line) and double (blue solid line) power-law for the SDSS, 2SLAQ and AAΩ LRGs. Lower panels show the fitting residuals for the single (circles) and double (triangles) power-law.

Table 2. Parameters for the power-law fits to the angular correlation function derived from three LRG samples. The best-fit parameters given are defined such that $w(\theta) = (\theta/\theta_0)^{1-\gamma}$ and $\xi(r) = (r/r_0)^{-\gamma}$. Also given are the corresponding 1σ error for each parameter.

Sample	Single power-law			Double power-law		
	$\theta_0(^{\circ})$	γ	$r_0(h^{-1} \text{ Mpc})$	$\theta_0(^{\circ})$	γ	$r_0(h^{-1} \text{ Mpc})$
SDSS	1.69 ± 0.03	2.07 ± 0.01	8.70 ± 0.09	1.57 ± 0.05	2.19 ± 0.03	7.35 ± 0.08
				1.05 ± 0.09	1.85 ± 0.04	9.15 ± 0.16
2SLAQ	0.87 ± 0.01	2.01 ± 0.01	7.50 ± 0.04	0.83 ± 0.01	2.16 ± 0.01	6.32 ± 0.03
				0.60 ± 0.03	1.84 ± 0.02	7.78 ± 0.05
AAΩ	0.57 ± 0.01	1.96 ± 0.01	7.56 ± 0.03	0.56 ± 0.01	2.14 ± 0.01	5.96 ± 0.03
				0.38 ± 0.02	1.81 ± 0.02	7.84 ± 0.04

pected. This is simply because the SDSS LRG sample is intrinsically more luminous than the 2SLAQ and AAΩ LRG samples and is not an indication of evolution.

To this end, we cut back the faint magnitude limit of 2SLAQ and AAΩ LRG's to $i_{\text{dev}} < 19.32$ and 20.25, respectively. These cuts are imposed in order to select the samples of Early-type galaxies whose comoving number densities are approximately matched to that of the SDSS LRG ($n \sim 7 \times 10^{-5} h^3 \text{ Mpc}^{-3}$). The $K + e$ corrected i -band absolute magnitudes of these samples are presented in Fig. 10. We see that their absolute magnitudes are also approximately matched. This would then allow us to roughly constrain the evolution of LRG clustering up to $z \sim 0.68$ (see §5). A summary of the properties of these samples and the best-fit parameters are given in Table 3. The measured $w(\theta)$'s are shown in Fig. 11a.

As expected, the amplitudes of the brighter cut 2SLAQ and AAΩ samples (denoted by 2SLAQ* and AAΩ* hereafter) are higher than the original sample. In its raw form, $w(\theta)$ measured from 2SLAQ* increases relative to 2SLAQ more than AAΩ relative to AAΩ*, due to the narrower redshift distribution of the 2SLAQ* sample. However, if we per-

form a double power-law fit to these results, the large-scale, $\gtrsim 1 h^{-1} \text{ Mpc}$, clustering lengths are very similar and agree within $\sim 1\sigma$ statistical error. To first order these large-scale clustering lengths are also consistent with that of the SDSS LRG's. We shall investigate the clustering evolution of these LRG samples further in §5.

4.2 Comparison of the clustering form to the standard Λ CDM model

We shall compare our $w(\theta)$ measurements to the predictions of the standard Λ CDM model in the linear perturbation theory of structure growth framework along with the non-linear correction. For the theoretical models, we first generate matter power spectra, using the 'CAMB' software (Lewis, Challinor & Lasenby 2000). In the case of non-linear correction, the software has the 'HALOFIT' routine (Smith et al. 2003) implemented. Such matter power spectra, $P_m(k, z)$, are then output at the average redshift of each sample. The matter correlation function, $\xi_m(r)$, is then obtained by Fourier transforming these matter power spectra using

Table 3. Properties and the best-fit parameters for double power-law of $w(\theta)$ measured from the SDSS-density matched samples.

Sample	number	magnitude	\bar{z}	n ($h^3 \text{ Mpc}^{-3}$)	Double power-law	
					$r_0(h^{-1} \text{ Mpc})$	γ
2SLAQ*	182 841	$17.5 < i_{\text{deV}} < 19.32$	0.53	$\sim 6.5 \times 10^{-5}$	6.33 ± 0.04 8.88 ± 0.08	2.25 ± 0.02 1.80 ± 0.02
AA Ω^*	374 198	$19.8 < i_{\text{deV}} < 20.25$	0.67	$\sim 7.1 \times 10^{-5}$	6.25 ± 0.03 9.08 ± 0.06	2.20 ± 0.02 1.76 ± 0.03

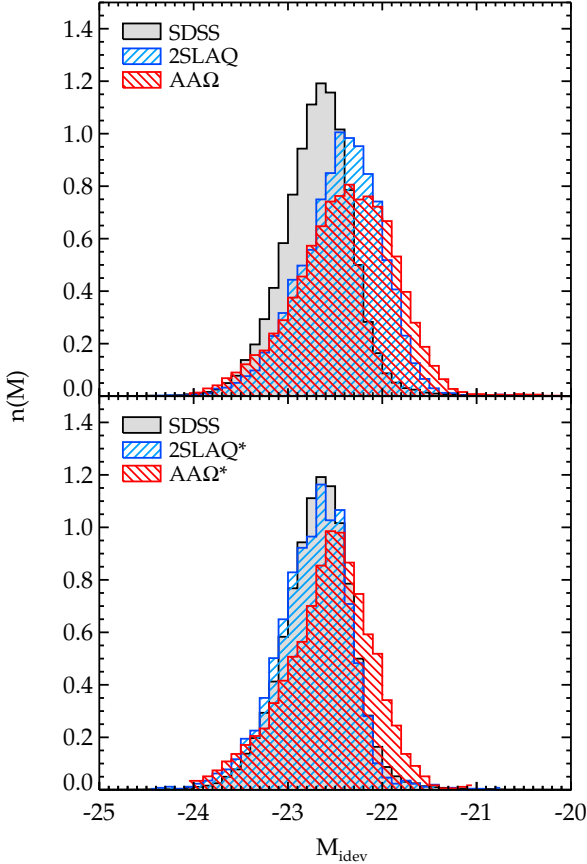


Figure 10. *Top:* The i -band absolute magnitude distribution of the spectroscopic LRG catalogues. All photometry is galactic-extinction corrected using dust map of Schlegel, Finkbeiner & Davis (1998) and $K+e$ corrected to $z=0$ using the Early-type galaxy templates from Bruzual & Charlot (2003). *Bottom:* The distribution of the absolute magnitude after applying a faint limit cut to 2SLAQ and AA Ω LRG in order to match the comoving number density of the SDSS LRG.

$$\xi_m(r) = \frac{1}{2\pi^2} \int_0^\infty P_m(k) k^2 \frac{\sin kr}{kr} dk \quad (17)$$

Under the assumption that galaxies trace dark matter haloes, the galaxy correlation function, $\xi_g(r)$, is related to the underlying dark matter by the bias factor, b_g , via

$$b_g^2 = \frac{\xi_g(r)}{\xi_m(r)} \quad (18)$$

Therefore the bias factor is expected to be a function of scale unless galaxies cluster in exactly the same manner as the

dark matter does at all scales. However, if we go out to large enough scales, i.e. the linear regime, the bias factor is approximately scale-independent over possibly a decade of scales.

Although, we found the clustering lengths and hence the amplitude of $\xi(r)$ to be very similar for the SDSS, 2SLAQ* and AA Ω^* samples, the evolution in the dark matter clustering means that the linear bias could be a strong function of redshift as we shall see in the next section where we investigate the clustering evolution in more detail. The evolution of structures in linear theory framework is described by the linear growth factor, $D(z)$, (e.g. Peebles 1984; Carroll et al. 1992) such that

$$\delta(r, z) = D(z)\delta(r, z=0), \quad (19)$$

recall that $\xi(r) = \langle \delta(\mathbf{r}_1) \delta(\mathbf{r}_2) \rangle$, where $r = |\mathbf{r}_1 - \mathbf{r}_2|$, then

$$\xi_m(r, z) = D^2(z)\xi_m(r, 0) \quad (20)$$

The linear growth factor is unity at the present epoch, by definition, and decreases as a function of redshift. The $\xi_m(r, z)$ therefore decreases as the redshift increases hence given that the number-density/luminosity matched samples have similar $\xi_g(r)$ amplitudes suggests that the bias increases as a function of redshift.

We proceed by projecting the predicted $\xi_m(r)$ using Eq. 13. Our fiducial models assume a Λ CDM Universe with $\Omega_\Lambda = 0.73$, $\Omega_m = 0.27$, $f_{\text{baryon}} = 0.167$, $\sigma_8 = 0.8$, $h = 0.7$ and $n_s = 0.95$. The linear bias factor is then estimated by fitting the matter $w(\theta)$ to the measured values for the comoving separation of $\sim 10\text{--}40 h^{-1} \text{ Mpc}$. The best-fit linear biases for all the LRG samples are given in Table 4. Note that the bias values estimated in this way seems to be ~ 10 per cent higher than our alternative method discussed in §5. To first order, these biases are compatible with the measurements from other authors (see e.g. Tegmark et al. 2006; Ross et al. 2007; Padmanabhan et al. 2007; Blake et al. 2007)

Fig. 11b shows the full scaling of the $w(\theta)$'s, accounting for their survey differences. First, the $w(\theta)$ of the SDSS, and 2SLAQ* samples scaled in the angular direction according to their average redshifts and relative to the AA Ω^* sample. The amplitudes are then scaled to obtain a fair comparison for samples with different redshift distributions. This is done by taking the relative amplitudes of the projections of a power-law $\xi(r)$ of the same clustering strength but projected through different $n(z)$ widths. Since the observed large-scale clustering lengths are very similar, $\sim 9 h^{-1} \text{ Mpc}$, the scaled $w(\theta)$'s in these ranges agree reasonably well. The figure also shows the best-fit model for the AA Ω^* sample and its non-linear correction. Our $w(\theta)$ shapes in the ranges $4 \lesssim r \lesssim 50 h^{-1} \text{ Mpc}$ can be described very well by the

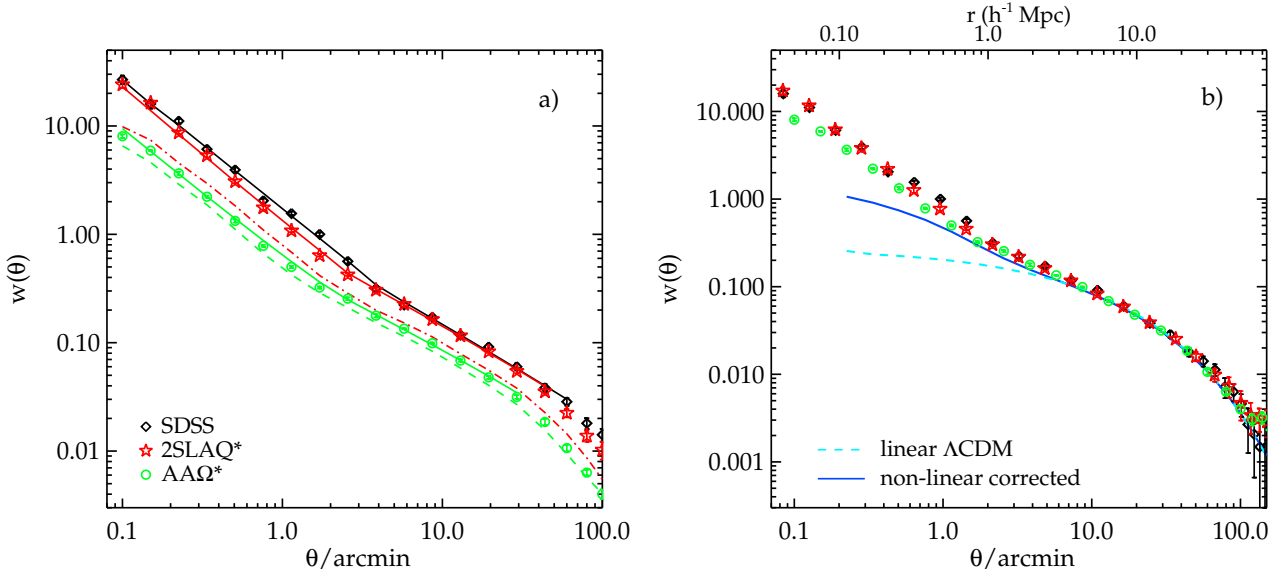


Figure 11. (a): The angular correlation function measured from the SDSS LRG and the brighter magnitude limit samples drawn from 2SLAQ and AAΩ sample (symbols). The solid lines are the projection of the best-fit double power-law $\xi(r)$ with the parameters shown in Table 3. For comparison, the dot-dashed and dashed lines are $w(\theta)$ measured from the whole 2SLAQ and AAΩ samples, respectively. (b): Same as (a) but now scaled to AAΩ depth and taking into account the relative amplitude due to the different $n(z)$ widths (see text for more details).

linear perturbation theory in the standard flat Λ CDM Universe. However, at scales $\lesssim 4 h^{-1}$ Mpc, the linear theory underestimates the clustering amplitude, as expected. The discrepancy between the linear theory is reduced when the non-linear correction of Smith et al. (2003) is applied.

5 EVOLUTION OF LRG CLUSTERING AND DARK MATTER HALO MASSES

5.1 Intermediate scales

5.1.1 Clustering evolution

In this section, we make an attempt to quantify the clustering evolution of the LRGs via the use of the $w(\theta)$'s measured from the number-density (roughly luminosity) matched samples as presented in the last section. We shall first compare the result at the intermediate scales, $1 \gtrsim r \gtrsim 20 h^{-1}$ Mpc, to the simple long-lived model of Fry (1996). The model assumes that galaxies are formed at a particular time in the past and their clustering evolution is determined by the influence of gravitational potential where no galaxies are destroyed/merged or new population created, hence preserving the comoving number density. In such a model the galaxy linear bias is given by

$$b(z) = 1 + \frac{b(0) - 1}{D(z)} \quad (21)$$

and as we saw in §4.2 that $\xi_m(r, z) = D^2(z)\xi_m(r, 0)$, the clustering evolution is such that

$$\xi_g(r, z) = \left[\frac{b(0) + D(z) - 1}{b(0)} \right]^2 \xi_g(r, 0) \quad (22)$$

We shall also compare the data directly to the linear theory prediction for dark matter evolution in the Λ CDM

model, $\xi(r, z) \propto D^2(z)$. In addition, we shall also check the stable clustering and no-evolution (comoving) clustering models of Phillipps et al. (1978). The stable model refers to clustering that is virialised and therefore stable in proper coordinates. For a $\xi(r)$ with r measured in comoving coordinates, the stable model has evolution $\xi(r) \propto (1+z)^{\gamma-3}$ and the no-evolution model has $\xi(r)$ independent of redshift. At these intermediate scales, the clustering is unlikely to be virialised so the stable model is shown mainly as a reference point. From Eq. 22, the no-evolution model represents the high bias limit of the long-lived model of Fry (1996). The stable and comoving models are similar to the long-lived model in that they both assume that the comoving galaxy density remains constant with redshift.

In order to quantify the clustering amplitude of each sample, we shall use the integrated correlation function in a $20 h^{-1}$ Mpc sphere as also utilised by several authors (e.g. Croom et al. 2005; Ross et al. 2008; da Ångela et al. 2008). The volume normalisation of this quantity is then given by

$$\xi_{20} = \frac{3}{20^3} \int_0^{20} \xi(r) r^2 dr \quad (23)$$

The $20 h^{-1}$ Mpc radius is chosen to ensure a large enough scale for linear theory to be valid and in our case the power-law with $\gamma \sim 1.8$ remains a good approximation up to $\sim 20 h^{-1}$ Mpc. Furthermore, the non-linearity at small scales does not significantly affect the clustering measurements, when averaged over this range of scales.

The integrated correlation function, ξ_{20} , approach also provides another means of measuring the linear bias of the sample. For this, we again assume scale-independent bias which is a reasonable assumption in the linear regime. The bias measured in this way is given by

Table 4. Summary of the estimated LRG and 2dFGRS early-type galaxy linear bias and M_{DMH} as a function of redshift and luminosity.

Sample	\bar{z}	\bar{M}_i $-5 \log_{10} h$	b_{lin} (ξ_{20})	M_{DMH} ($10^{13} h^{-1} M_{\odot}$)	b_{lin} ($10-40 h^{-1} \text{Mpc}$)
SDSS	0.35	-22.67	2.02 ± 0.04	4.1 ± 0.3	2.10 ± 0.04
2SLAQ*	0.53	-22.69	2.16 ± 0.04	3.3 ± 0.2	2.26 ± 0.04
AAΩ*	0.67	-22.60	2.33 ± 0.03	3.1 ± 0.1	2.37 ± 0.03
2SLAQ	0.55	-22.40	1.91 ± 0.03	2.1 ± 0.1	1.99 ± 0.02
AAΩ	0.68	-22.37	2.04 ± 0.02	1.9 ± 0.1	2.20 ± 0.02
N02E1	≈ 0.1	-22.68	1.90 ± 0.23	6.2 ± 2.2	—
N02E2	≈ 0.1	-22.40	1.66 ± 0.20	3.9 ± 1.5	—

$$b_g(z) = \sqrt{\frac{\xi_{20,g}}{\xi_{20,m}}} \quad (24)$$

The mass integrated correlation functions are again computed assuming our fiducial cosmological model using the matter power spectra output from CAMB. The values for $\xi_{20,m}$ used here are 0.153, 0.126 and 0.112 for $z = 0.35$, 0.55 and 0.68, respectively.

The $\xi_{20,g}$ is calculated using the best-fit double power-law parameters for each sample. The results are plotted in Fig. 12a along with the best-fit linear theory evolution (long-dashed line), stable clustering (dotted line), long-lived (dashed line) and no-evolution models (dot-dot-dashed line). The linear biases measured using the ξ_{20} approach are given in Table 4 and also presented in Fig. 12b. As mentioned earlier, the bias values measured in this way seem to be ~ 10 per cent systematically lower than the best-fit values. Throughout this section, we shall use the values obtained from the ξ_{20} approach to remain consistent.

To extend the redshift range, we shall compare our results to the clustering of early-type galaxies in 2dFGRS studied by Norberg et al. (2002) that roughly match the absolute magnitude of our samples after the $K + e$ correction. These are the samples with $-21.0 > M_{b_j} - 5 \log_{10} h > -22.0$ and $-20.5 > M_{b_j} - 5 \log_{10} h > -21.5$, being compared to the SDSS/2SLAQ*/AAΩ* and 2SLAQ/AAΩ data and denoted N02E1 and N02E2 in Table 4, respectively. We proceed in a similar fashion to the procedure described above and use the author's best-fit power-law to estimate the $\xi_{20,g}$'s and hence the bias values (see Table 4).

Both luminosity bins can be reasonably fitted by the long-lived model. The best-fit models for the $M_i - 5 \log_{10} h = -22.7$ and -22.4 samples have $b(0) = 1.93 \pm 0.02$ and 1.74 ± 0.02 with $\chi^2 = 7.34$ (3 d.o.f) and 4.11 (2 d.o.f) respectively, i.e. rejected at $1.5-1.9\sigma$ significance. This is interesting given the lack of number density evolution seen in the LRG luminosity function by Wake et al. (2006). Nevertheless, it is intriguing that such a simple model gets so close to fitting data over the wide redshift range analysed here.

The stable model and the linear theory (with constant bias) model rise too quickly as the redshift decreases, excluded at $> 99.99\%$ confidence. However, the comoving model also gives a good fit to the SDSS/2SLAQ*/AAΩ* data in Fig. 12a, as expected from the lack of evolution shown in Fig. 11b. For this model to be exactly correct it would suggest that there was an inconsistency in these results with the underlying Λ CDM halo mass function. More

certainly, we conclude that the evolution of the LRG clustering seems very slow. This general conclusion agrees with previous work (White et al. 2007; Wake et al. 2008). The latter author also only found a marginal rejection of the long-lived model from the large-scale galaxy distribution (1.8σ) compared to 1.9σ here. They found a much stronger rejection of a 'passive' evolution model from the small-scale LRG clustering and we shall return to this issue in §5.2.

5.1.2 LRG dark matter halo masses

The large-scale galaxy bias is roughly the same as that of the dark matter haloes which is a known function of mass threshold. Thus by measuring the clustering of the LRGs one can infer the typical mass of the haloes they reside in. The procedure employed here is similar to that used by Croom et al. (2005) and da Ângela et al. (2008) to estimate the dark matter halo masses of QSOs.

An ellipsoidal collapse model relating a halo bias factor to its mass was developed by Sheth et al. (2001) as an improvement over an earlier spherical collapse model of Mo & White (1996). In this analysis, we shall use the expression given in Sheth et al. (2001) and the revised parameters of Tinker et al. (2005) which were calibrated to give better fits to a wide range of σ_8 values for variants of Λ CDM model;

$$b(M_{\text{DMH}}, z) = 1 + \frac{1}{\sqrt{a}\delta_c(z)} \left[\sqrt{a}(a\nu^2) + \sqrt{ab}(a\nu^2)^{1-c} - \frac{(a\nu^2)^c}{(a\nu^2)^c + b(1-c)(1-c/2)} \right], \quad (25)$$

where $a = 0.707$, $b = 0.35$ and $c = 0.80$. ν is defined as $\nu = \delta_c(z)/\sigma(M_{\text{DMH}}, z)$. δ_c is the critical density for collapse, and is given by $\delta_c = 0.15(12\pi)^{2/3}\Omega_m(z)^{0.0055}$ (Navarro et al. 1997). The rms fluctuation of the density field as a function of mass M_{DMH} at redshift z is $\sigma(M_{\text{DMH}}, z) = \sigma(M_{\text{DMH}})D(z)$ where $\sigma(M_{\text{DMH}})$ is given by

$$\sigma(M_{\text{DMH}})^2 = \frac{1}{2\pi^2} \int_0^\infty k^2 P(k) w(kr)^2 dk \quad (26)$$

$P(k)$ is the power spectrum of density perturbations and $w(kr)$ is the window function, given by (Peebles 1980)

$$w(kr) = 3 \frac{\sin(kr) - kr \cos(kr)}{(kr)^3}, \quad (27)$$

for a spherical top-hat function. The radius r can be related to mass via

$$r = \left(\frac{3M_{\text{DMH}}}{4\pi\rho_0} \right)^{1/3}, \quad (28)$$

where $\rho_0 = \Omega_m^0 \rho_{\text{crit}}^0$ is the present mean density of the Universe, given by $\rho_0 = 2.78 \times 10^{11} \Omega_m^0 h^2 M_{\odot} \text{Mpc}^{-3}$. Here, we use the transfer function, $T(k)$, fitting formula given by Eisenstein & Hu (1998) to construct $P(k)$, assuming our fiducial cosmology (see §4.2) and 'HALOFIT' routine (Smith et al. 2003) for the non-linear correction.

Note that the formalism of estimating dark matter halo masses from the galaxy biases used here assumes one galaxy per halo and can overestimate the mean M_{DMH} for a given value of bias, similar to the effect it has on the threshold mass (Zheng et al. 2007). This effect is worse for a low

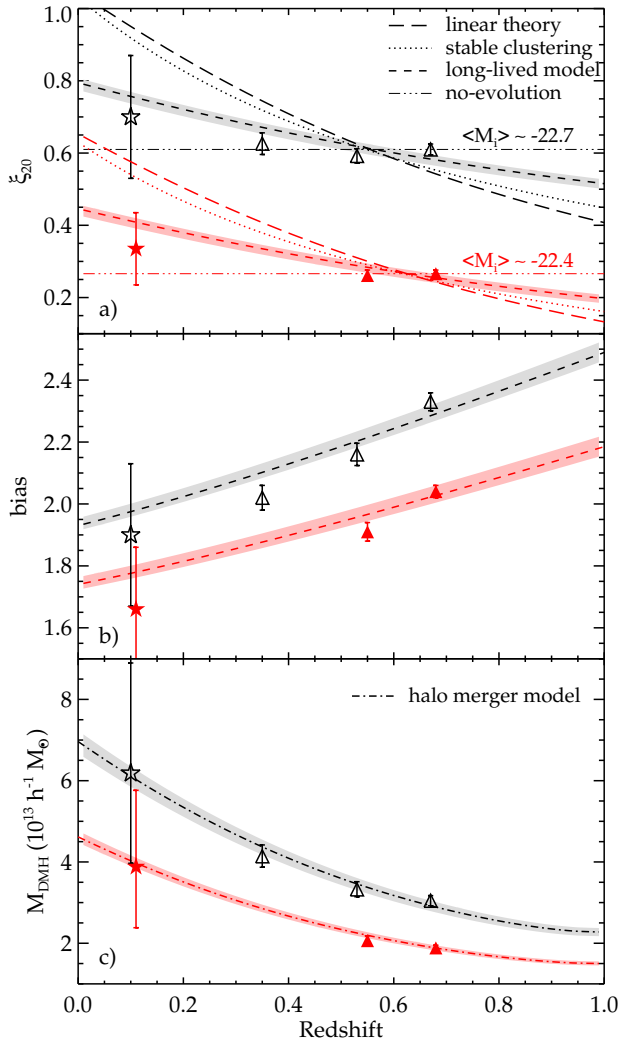


Figure 12. (a): The LRG ξ_{20} measurements as a function of redshift and luminosity. The data at $z \approx 0.1$ (stars) are taken from the correlation functions of early-type galaxies in 2dFGRS (Norberg et al. 2002). Open and solid symbols correspond to the samples with median absolute magnitude, $M_i - 5 \log_{10} h = -22.7$ (SDSS/2SLAQ*/AAΩ*) and -22.4 (2SLAQ/AAΩ). The best fits for various models are also shown (see text for more details). The lower luminosity data have been lowered by 0.2 for clarity. (b): The LRG linear biases as a function of redshift and luminosity, comparing to the best-fit long-lived model. (c): The typical mass of dark matter haloes occupied by the LRGs as estimated from the halo bias function. The dot-dashed lines are the best-fit evolution model of dark matter halo mass via the merger framework (Lacey & Cole 1993).

bias halo at high redshift. However for the range of LRG biases and redshifts considered here, the difference should be negligible (see Fig. 11 in Zheng et al. 2007). The estimated dark matter halo masses of the LRG samples are given in Table 4 and plotted in Fig. 12c. As expected, these LRGs reside in the most massive dark matter haloes, $M_{DMH} > 10^{13} h^{-1} M_\odot$, and increases as a function of luminosity, following their clustering strengths.

Next, we attempt to fit the derived dark matter halo

masses of these LRGs to the halo merger framework in hierarchical models of galaxy formation. We use the formalism discussed by Lacey & Cole (1993) to predict the median M_{DMH} of the descendants of virialised haloes at $z = 1$ for a given halo mass and fit this to our data. In essence, the model gives the probability distribution of the haloes with mass M_1 at time t_1 evolving into a halo of mass M_2 at time t_2 via merging. Fig. 12c shows the best-fit models for the M_{DMH} evolution estimated in this way. These models appear to be good fits to both luminosity bins with the best-fit $M_{DMH}(z = 1) = 2.32 \pm 0.07 \times 10^{13} h^{-1} M_\odot$ and $1.47 \pm 0.05 \times 10^{13} h^{-1} M_\odot$ for the $L \gtrsim 3L^*$ and $\gtrsim 2L^*$ samples, respectively.

The most massive haloes hosting these luminous early-type galaxies appear to have tripled their masses over the past 7 Gyr (i.e. half cosmic time) in stark contrast to the little evolution observed in the LRG stellar masses over the same period (see e.g. Wake et al. 2006; Cool et al. 2008). This lack of evolution contradicts the predictions in the standard hierarchical models of galaxy formation where one expects the most massive galaxies to form late via ‘dry’ merging of many less massive galaxies.

5.2 Small-scale clustering evolution

Finally, we discuss the evolution of the correlation function at scales corresponding to $r < 1 h^{-1} \text{Mpc}$. We concentrate on comparing the luminosity matched AAΩ* and 2SLAQ* samples to the SDSS sample. As can be seen in Fig. 11b, while at larger scales the $w(\theta)$ show amplitudes that are remarkably independent of redshift, at smaller scales the high redshift AAΩ* sample appears to have a lower amplitude than the lower redshift surveys. From the fits to the double power-laws in Tables 2 and 3 we estimate the correlation function at a fiducial separation of $0.5 h^{-1} \text{Mpc}$ for each survey and plot against redshift in Fig. 13. To these we add points representing the 2dFGRS survey early-types at $M_i - 5 \log_{10} h = -22.68$ at $z \approx 0.1$ (N02E1). We also add the measurement at $z = 0.28$ from the spectroscopic LRG sample with similar luminosity and comoving number density as ours ($-23.2 < M_{g,0.3} < -21.2$, Zehavi et al. 2005a). The errors on these points take into account the errors on both the amplitudes and slopes on the power-law fits. As expected, the points appear to show a trend towards lower amplitudes at higher redshift, particularly for the AAΩ* sample. We again compare these data to the stable/virialised and linear evolution models. We do not consider the long-lived model of Fry (1996) on the assumption that this only has applicability in the linear regime. The best-fit stable clustering model has $\xi_g(0) = 420 \pm 14$ and $\chi^2 = 6.15$ (4 d.o.f.), i.e. a marginal rejection of 1.3σ significance. The linear evolution with constant bias also gives a reasonable fit to the data. But the no-evolution model (not shown on the plot) seems to fit less well in this small-scale regime than at larger scales and is rejected at $> 99.9\%$ confidence.

The physical picture that is suggested is that the inflexion in the correlation function may represent the boundary between a virialised regime at small scales and a co-moving or passively evolving biased regime at larger scales. As noted by Hamilton et al. (1991) and Peacock & Dodds (1996), the small scale, non-linear, DM clustering is clearly expected from N-body simulations to follow the evolution

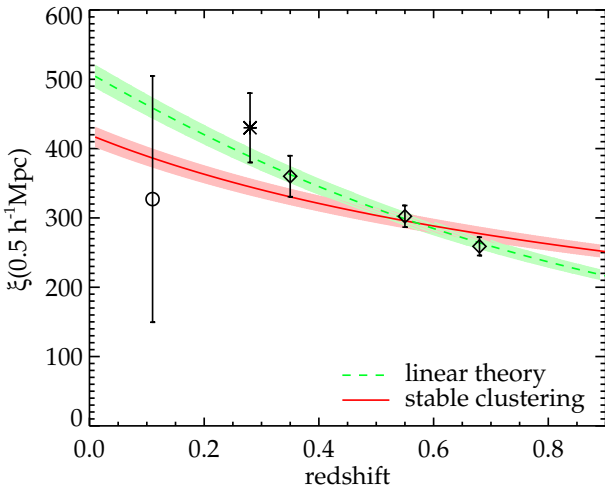


Figure 13. Clustering evolution at small scales, $r = 0.5 h^{-1} \text{Mpc}$. Our LRG number density matched samples, SDSS/2SLAQ*/AAΩ*, are shown as diamonds. These are compared to the 2dFGRS early-type galaxies (N02E1, open circle) and the SDSS LRG measurement at $z = 0.28$ (asterisk) by Zehavi et al. (2005a). The best-fit stable clustering and linear theory evolution, $\xi_g(z) \propto D^2(z)$, models are also shown.

of the virialised clustering model. However, for galaxies in an Λ CDM context, the picture may be more complicated. For example, by comparing the 2SLAQ and SDSS LRG redshift surveys using the semi-projected correlation function, Wake et al. (2008) have suggested that a passively evolving model is rejected, weakly from the large scale evolution but more strongly from the evolution at small scales. Wake et al. (2008) interpret the clustering evolution using a HOD description based on the Λ CDM halo mass function. Their ‘passive’ model predicts a far faster evolution at small scales than is given by our stable clustering and linear theory model - at $r = 0.5 h^{-1} \text{Mpc}$ the rise is $\sim 2.5 \times$ between $z = 0.55$ and $z = 0.19$ (see their Fig. 11). Indeed, otherwise, the observational LRG results of Wake et al. (2008) at both small and intermediate scales are quite consistent with our own. However, it should be noted that the colour selections between our LRG samples may be somewhat different and we have not attempted to match their colours exactly as it was done in Wake et al. (2008).

Our stable model is certainly passive in that it is based on the idea that the comoving number density of galaxies is independent of redshift. It will be interesting to see if another HOD prescription can be found which allows our observed stable galaxy clustering at small scales and passive evolution at larger scales to be consistent with the evolution of the Λ CDM halo mass function. Otherwise the virialised model may only provide a phenomenological fit to the small scale clustering evolution in the context of the Λ CDM model. If the passive HOD model of Wake et al. (2008) is more appropriate for the Λ CDM case then it suggests that only 7.5 per cent of LRGs need to merge between $z=0.55$ and $z=0.19$ to reconcile the slow LRG density and clustering evolution with the Λ CDM model. Again, it will be interesting to see

if this model can also accommodate our $z=0.68$ clustering result while maintaining such a low merger rate.

6 SEARCHING FOR THE BAO PEAK

Next, we inspect the correlation functions at larger scales to make a search for the BAO feature. We first present the raw correlation functions in Fig. 14. Each correlation shows feature at large scales; the question is are they real or simply due to systematic or statistical error? We therefore perform a classic scaling test to see if any feature is reproduced at the different depths of the three LRG samples. Given that the samples have intrinsically different r_0 (see Table 2), we choose simply to scale in the angular direction only. The SDSS and 2SLAQ LRG correlation functions are scaled in the angular direction to the AAΩ’s depth using the average radial comoving distance of each sample (see Fig. 15). Note that the apparent scaling below $100'$ is accidental because of the different r_0 ’s and $n(z)$ widths coincidentally cancelling out in their effects on $w(\theta)$. In Fig. 15, we see that the scaling agreement of the large scale features is poor. Although SDSS shows a strong peak feature, this is not reproduced at the same scale in the other two datasets.

The poor scaling could be regarded as an indication that the feature seen in the SDSS sample was false. Support for this view comes from the fact that the other two samples show some evidence of a feature at the same (angular) scale as the SDSS. This could indicate that this feature is actually an artefact even in the SDSS data. With this view, then it is easy to estimate how much extra power might be added at the $100 h^{-1} \text{Mpc}$ peak by such an artefact in the angular direction. At $100 h^{-1} \text{Mpc}$ the $\xi(s)$ model from Eisenstein et al. (2005) has $\xi(s) = 0.01$ and at the equivalent angular scale the possibly spurious angular peak has $w(\theta) = 0.003$. Thus the overall peak has perhaps been overestimated by 30 per cent due to this angular feature. This would reduce the significance of the peak in $\xi(s)$ from $\sim 3\sigma$ to $\sim 2\sigma$, although a coincidence would also be demanded between the angular and redshift directions, since the angular direction’s contribution is still sub-dominant.

Despite this failure of the scaling test, we now attempt to increase the signal to noise ratio by combining the measurements from the three samples using the inverse quadrature error weighting. Firstly, the SDSS and 2SLAQ $w(\theta)$ ’s are scaled in the angular direction to the depth of the AAΩ LRGs (radial comoving distance, $\chi \approx 1737 h^{-1} \text{Mpc}$ as opposed to $\approx 1451 h^{-1} \text{Mpc}$ for 2SLAQ and $\approx 970 h^{-1} \text{Mpc}$ for SDSS) where their amplitudes and errors are then interpolated to the AAΩ’s angular bins. Hence we are exploiting the coincidental approximate cancellation between the r_0 differences and the $n(z)$ widths which have left the small scale $w(\theta)$ ’s reasonably, if accidentally, in agreement. The resulting correlation function is presented in Fig. 16. Note that due to the relatively small statistical errors of the AAΩ LRG compared to other samples, the $w(\theta)$ result is dominated by the AAΩ sample, therefore the possible SDSS peak at $\sim 100 h^{-1} \text{Mpc}$ is not evident in the combined sample. There also seems to be an indication of an excess out to possibly $200 h^{-1} \text{Mpc}$, although statistical (and systematic) errors are large in this region.

Using the ubercalibration (Padmanabhan et al. 2008)

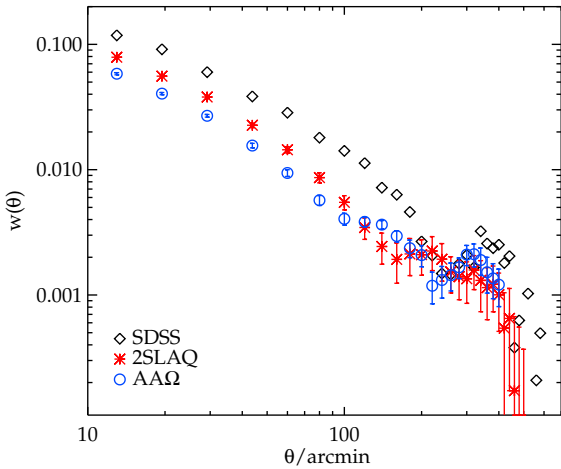


Figure 14. The angular correlation function of the three LRG samples at large scales. The statistical errors of the SDSS are not shown for clarity.

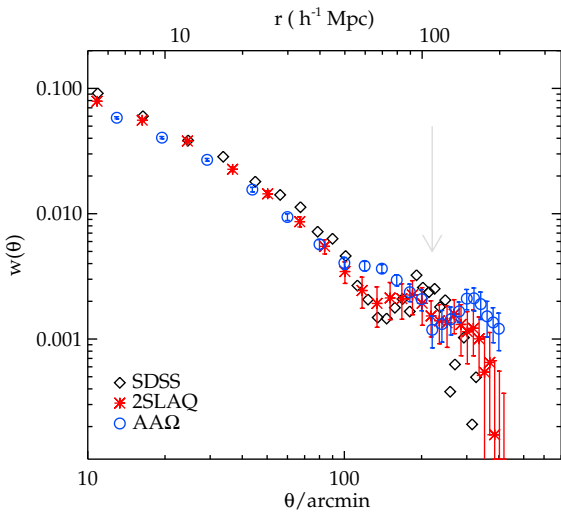


Figure 15. The angular correlation function of the three LRG samples scaled in the angular direction to the depth of AAΩ LRG. The arrow indicates the expected scale of the BAO peak in the scaled angular correlation functions.

instead of the standard calibration, we find similar results at small and intermediate scales but a slightly lower amplitude at the scales around $100 h^{-1}$ Mpc although the results agree within the 1σ error (see Fig. 16). This means the correlation functions at small and intermediate scales including the parameters derived (e.g. power-law fits, linear biases, dark matter halo masses) in the earlier parts are not affected by which calibration we use. The biggest difference is observed at scales larger than $100 h^{-1}$ Mpc and up to $200 h^{-1}$ Mpc where the correlation signal is small and hence more prone to possible systematics. The dependence of the $w(\theta)$ amplitudes on the different calibrations may be an indication that this apparent extra peak at $\theta \approx 300'$ could

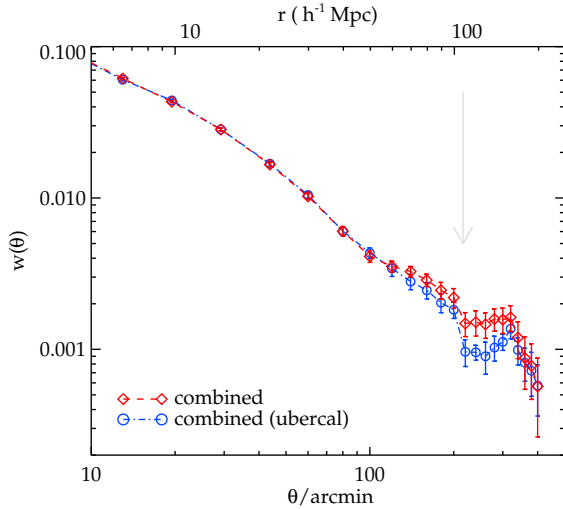


Figure 16. The combined angular correlation function of the three LRG samples comparing the results when the SDSS standard (diamonds) and uber- (circles) calibration are used.

indeed be an artefact. Hereafter, we shall use the correlation function measured from the sample selected using ubercalibration and shall return to discuss this possible systematic in §6.1.

6.1 Model comparisons

Next, we shall compare the aforementioned combined angular correlation function (w_{com} hereafter) of the LRG samples to the prediction of the perturbation theory in the standard Λ CDM Universe. To compute the theoretical prediction, we proceed in the same manner as described in §4.2, calculating $w(\theta)$ by projecting $\xi(r)$ which is a Fourier transform of a non-linear $P(k)$, assuming our fiducial cosmology. Fig. 17 shows w_{com} along with this flat Λ CDM theoretical prediction (red solid line). We find that although the results are consistent with the standard model at scales $\lesssim 50 h^{-1}$ Mpc (see also §4.2), the w_{com} above this scale has a higher clustering amplitude than the theoretical expectation. As a result, the peak feature at $\approx 100 h^{-1}$ Mpc appears to be inconsistent with the model.

Next, we wish to compare the w_{com} to a projected polynomial-fit of the previous BAO detection at $z \approx 0.35$ by Eisenstein et al. (2005). This model is computed by projecting the de-boosted redshift-space correlation function, $\xi(s)$. In the linear regime, due to the coherent infall around clusters, the $\xi(s)$ amplitude is enhanced relative to the real-space correlation function, $\xi(r)$, such that (Kaiser 1987)

$$\xi(s) = \left(1 + \frac{2\beta}{3} + \frac{\beta^2}{5} \right) \xi(r). \quad (29)$$

Here, we shall assume $\beta = 0.40$ for the $z \approx 0.35$ LRG sample (see Ross et al. 2007). The de-boosted $\xi(r)$ is then corrected for the linear growth between $z = 0.35$ and $z = 0.68$ (see Eq. 20) which reduces the amplitude in the linear regime by ≈ 30 per cent. The resulting polynomial fitted model is shown as a blue dashed line in the inset of Fig. 17. This 3-D model of the Eisenstein et al. (2005) data is then projected

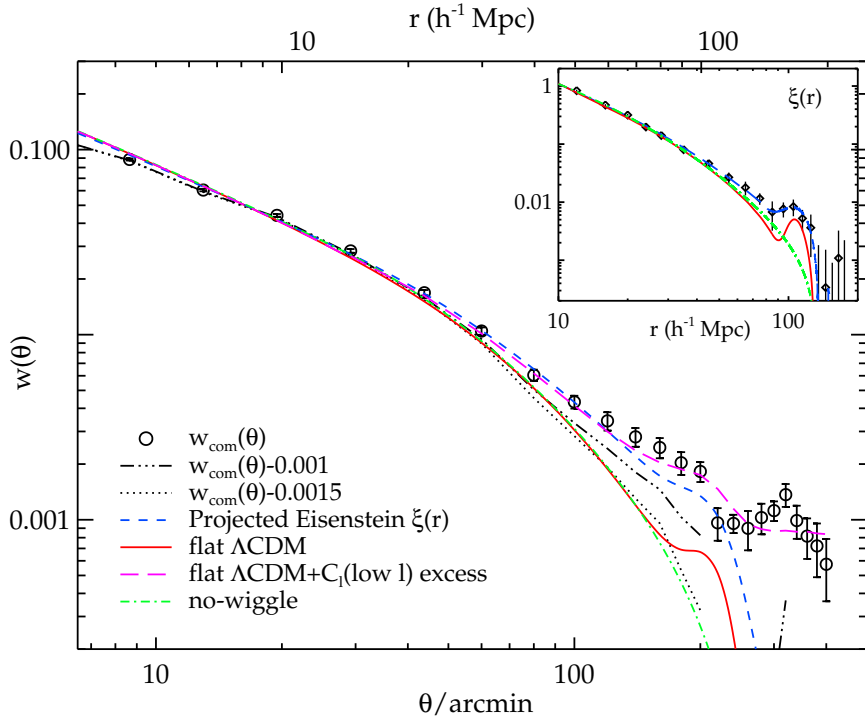


Figure 17. The combined $w(\theta)$ (open circles) compared to the projections of the flat Λ CDM model (red solid line), the Eisenstein et al. (2005) $\xi(r)$ (blue dashed line) and the no-wiggle model (dot-dashed line). The dash-dot-dotted and dotted line shows the effect of subtracting the data by 0.001 and 0.0015, respectively. The $\xi(r)$ models used in the Limber projection are given as an inset together with the Eisenstein et al. (2005) measurement (diamonds). Here, the same symbols are used for the Eisenstein et al. (2005), flat Λ CDM and no-wiggle $\xi(r)$ models as for the $w(\theta)$ models above.

to $w(\theta)$ using Eq. 13. The resulting model is shown by the blue dashed line in Fig 17. Our result appears to be in good agreement with this model up to $\sim 120 h^{-1}$ Mpc where w_{com} starts to rise and has a second peak at $\sim 200 h^{-1}$ Mpc whilst the model has a sharp drop beyond this scale.

Summarising, the w_{com} result appears to agree with the $w(\theta)$ prediction based on the Eisenstein et al. (2005) observed $\xi(s)$ but not with the prediction based on the flat Λ CDM model. Clearly, this seems to imply there is a contradiction between the Eisenstein et al. (2005) result and standard model in the sense that the former is too high. This is most apparent in the $w(\theta)$ results but also seen as a difference between the $\xi(r)$ results shown in the inset of Fig. 17 (dashed and solid lines).

Fig. 17 also compares w_{com} to the ‘no wiggle’ model (Eisenstein & Hu 1998). This should allow us to estimate the significance of the detection of any BAO feature in w_{com} . Out to 200', the w_{com} appears higher than the no-wiggle model by a significant amount. Given the good agreement between our measurement and Eisenstein et al. (2005) BAO, this could be taken as evidence that the BAO peak is being detected in the w_{com} at high significance. However, the difference between the no-wiggle $w(\theta)$ and the flat Λ CDM $w(\theta)$ is much smaller and would imply that the effect of the acoustic peak is expected to be much smaller. This ambiguity in the size of the effect on $w(\theta)$ due to the acoustic peak is clearly caused by the difference between the Eisenstein et al. (2005) $\xi(r)$ and the Λ CDM prediction.

The discrepancy between the Eisenstein et al. (2005) $\xi(r)$ and the Λ CDM prediction seen in Fig. 17 which re-

mains unexplained and is independent of any data presented here, since it already appears in $\xi(r)$ (Fig. 17 inset). Although the contrast of the acoustic peak could be smeared out by some non-linear processes which scatter galaxy pairs at $\approx 100 h^{-1}$ Mpc scale, the BAO peak amplitude is still too high for the Λ CDM prediction even with the non-linear correction used here, HALOFIT. The agreement between the observed peak amplitude and the theoretical prediction can be improved by increasing the baryon fraction at the expense of poorer fit at smaller scales (see Fig. 2 and 3 in Eisenstein et al. 2005).

If we now take another approach and take the excess signal at $\approx 200 h^{-1}$ Mpc as an indication of a systematic and subtract 0.001 to 0.0015, the level of the excess amplitude at this point in w_{com} (see Fig. 17), we obtain the $w(\theta)$ results as shown by the dash-dot-dotted and dotted lines. These two lines now bracket the flat Λ CDM result but clearly cannot exclude the no-wiggle model. Thus we conclude that the acoustic peak predicted by the basic standard Λ CDM model is undetectable in our data if the excess at large scales is interpreted as being due to systematics. Indeed, it could be said that if our normalisation of the Λ CDM model is correct then the amplitude of the acoustic peak is probably too low to be detected in any feasible projected LRG $w(\theta)$.

We note that Blake et al. (2007) and Padmanabhan et al. (2007) have also found an excess in their angular power spectrum, C_l , at $l < 10$ relative to the best-fit Λ CDM models, using photometric-redshift catalogues of the LRGs at $z \sim 0.5$. To estimate the effect of this low l excess on the angular correlation function,

we assume the extra power at $l < 10$ as observed by Blake et al. (2007). We compute the expected $w(\theta)$ via C_l in the standard Λ CDM Universe (§4.2), using the formalism, essentially Eqs. 10 and 14 for $C_{gg}(l)$, of Sawangwit et al. (2009). The excess power is modelled as a power-law at $l \lesssim 10$ and is truncated at $l \lesssim 1$. The result is shown in Fig. 17 as a long-dashed line. We find a good agreement with our angular correlation function. However, the fact that the excess power in the C_l taken the form of an $l < 10$ spike, suggests that this excess in $w(\theta)$ is due to an artefact or at least something other than acoustic oscillations in the power spectrum. If this spike is assumed to be an artefact (although see Yoo et al. 2009) then it would suggest that our offset subtracted $w(\theta)$ result is more correct although the offset as considered here is a weak function of scale. This would also imply that the agreement of our $w(\theta)$ with the Eisenstein et al. (2005) $\xi(s)$ result was accidental. We have already discussed in §6, the possible contribution of a 2-D artefact to the SDSS $z \approx 0.35$ $\xi(s)$ and if this C_l interpretation is correct then this possibility may be worth further consideration.

In summary, if the Eisenstein et al. (2005) $\xi(r)$ is correct then we may have already detected the BAO feature in our LRG $w(\theta)$. However if the flat Λ CDM is correct then our result is too much dominated by systematics at large scales to detect the acoustic peak. The crucial issue is the difference between the observed Eisenstein et al. (2005) $\xi(r)$ and the flat Λ CDM model. This difference even seems accentuated in $w(\theta)$ as opposed to $\xi(r)$. *If we take the evidence from the C_l that our $w(\theta)$ excess at scales beyond 100' is produced by the excess in the C_l at $l < 10$ and if we assume that this excess is an artefact, then we conclude a) that our $w(\theta)$ excess is not caused by the BAO as detected by Eisenstein et al. (2005), b) that the agreement with the Eisenstein et al. (2005) result is simply accidental and c) that our $w(\theta)$ result is more compatible with the flat Λ CDM model.*

Clearly, if the flat Λ CDM model with our normalisation is correct then the acoustic peak signal will be more difficult to detect with a foreseeable improvement in our data. We next discuss whether using a photometric LRG sample with narrower $n(z)$ through photo-z or an improved colour magnitude cut in future surveys can provide better chances for detecting the acoustic peak in LRG $w(\theta)$.

6.2 Future improvement

Finally, we shall investigate the effects the redshift distribution width has on the detectability of the BAO peak in angular correlation functions. For this purpose, we compute $w(\theta)$ by projecting the real-space correlation function using Eq. 13 with various galaxy redshift distributions. We use the observed $\xi(r)$ form rather than the Λ CDM prediction from CAMB or CMBfast because some non-linear effects could smear out the acoustic peak in a way that the non-linear correction such as HALOFIT (Smith et al. 2003) could not account for (see Fig. 17). For the observed $\xi(r)$, we use a fit of the de-boosted Eisenstein et al. (2005) LRG $\xi(s)$ assuming Kaiser factor, $\beta = 0.4$ in the linear regime, $r \geq 15 h^{-1}$ Mpc, and a power-law with $r_0 = 10.5 h^{-1}$ Mpc and $\gamma = 1.9$ for $r < 15 h^{-1}$ Mpc (Zehavi et al. 2005a). This model is shown as a dashed line in the inset of Fig. 17. To compare our

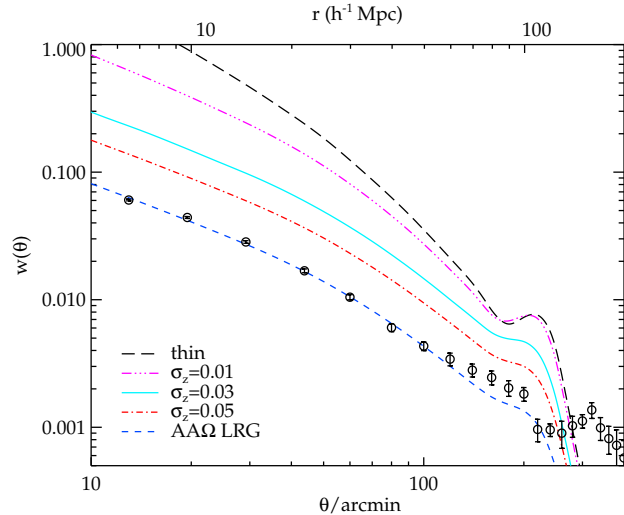


Figure 18. The angular correlation functions from the projected LRG $\xi(r)$ of Eisenstein et al. (2005) assuming different $n(z)$ widths. Our $w(\theta)$ measurement is also shown (diamonds) along with its expectation.

$w(\theta)$ measurement to the predicted photo-z result with redshift error, σ_z , we model the $n(z)$ as a Gaussian with width σ_z and average $z = 0.68$. We calculate the expected $w(\theta)$'s assuming the AA Ω LRG $n(z)$, $\sigma_z = 0.01, 0.03$ and 0.05 .

The results are shown in Fig. 18. The narrower $n(z)$ gives a higher $w(\theta)$ amplitude and steeper power-law slope as expected. This is because there are less galaxy pairs separated by different spatial scales in different redshift slices that project on to the sky at similar angular separation to dilute the spatial clustering signal. With a sufficiently small $n(z)$, $w(\theta)$ converges to the spatial correlation function as shown in Fig. 18 for the thin-layer approximation.

The thin-layer model is calculated by using an infinitesimally thin galaxy selection function, in this case a delta function, $\delta(z - 0.68)$, centred at the same redshift as the mean of the Gaussian $n(z)$. The result is an angular rescaling, corresponding to the radial comoving distance out to $z = 0.68$, i.e. $w(\theta) = \xi(\chi\theta)$. This is shown as a long-dashed line in Fig. 18. The BAO peak appears at $w \approx 0.01$, the same amplitude as the input $\xi(r)$ shown in the inset to Fig. 17. Clearly it would not make sense to pursue the angular correlation function route when the photo-z accuracy becomes much smaller than the BAO scale because at that point it will start to be advantageous to include the BAO signal from the radial direction as well as the angular direction by using either the 3-D correlation function, $\xi(s)$, or the semi-projected correlation function, $w(r_p)$. Thus for the approach we have followed here, the results in Fig. 18 corresponding to $\sigma_z \approx 0.03 - 0.05$ (i.e. $\Delta r \approx 60 - 100 h^{-1}$ Mpc) are the best the 2-D correlation functions can do. However, such a factor of $2\times$ improvement in the photo-z or colour-cut accuracy would be useful for the increased signal with respect to the systematic noise shown by the SDSS data in Fig. 18. Also with $\sigma_z = 0.03 - 0.05$ the signal to noise ratio is within a factor 1.5-2 of its best value in a spectroscopic survey in our redshift range (see Fig. 18).

The AA Ω LRG $n(z)$ can be narrowed down by the use of photo-z as opposed to using the simple colour-magnitude

cut considered in this study. The current best photo-z accuracy for $z \sim 0.5$ LRGs using the SDSS photometry with the Neural Networks algorithm gives $\sigma_z \approx 0.05 - 0.06$ (Collister et al. 2007; Abdalla et al. 2008), a modest improvement over what we currently achieve. But by combining with near-infrared photometry and a spectroscopic redshift training set of a few thousands, the photo-z accuracy of the AAΩ LRGs could be further improved, possibly to achieve the $\sigma_z = 0.03$ limit for the usefulness of the 2-D correlation function technique. The southern VST ATLAS and VISTA VHS surveys will double the area with optical-NIR photometry to search for BAO. The inclusion of NIR data from VISTA VHS survey is also expected to improve the photo-z accuracy (Banerji et al. 2008) of the proposed Dark Energy Survey (DES). The deeper grizy photometry of the Panoramic Survey Telescope and Rapid Response System (Pan-STARRS, Chambers 2009) 3π survey combined with the JHK photometry from the the UKIRT Infrared Deep Sky Survey (UKIDSS, Lawrence et al. 2007) Large Area Survey (LAS) should also give a photo-z accuracy of $\sigma_z(z = 0.7) \gtrsim 0.03$ (Cai et al. 2009). These improved photometric redshifts and the application of the full Limber's formula used here should also reduce any systematics in estimating the BAO scale (see Simpson et al. 2009) from this new generation of 2-D cosmological surveys.

7 SUMMARY AND CONCLUSIONS

We have presented here a new and detailed analysis of the angular correlation function of the Luminous Red Galaxies extracted from the SDSS DR5 photometric catalogue. All the necessary information for inferring the spatial clustering are obtained and calibrated through redshift surveys of the sample subset. Our conclusions are as follows;

- We measured the angular correlation function of the LRGs at three different redshifts, namely 0.35, 0.55 and 0.68 and found the results to be well approximated by power-laws at small and intermediate scales.
- With the large samples in terms of the numbers of objects and volume cover by the data, we see the deviation from the canonical single power-law at high significance.
- The data are better fitted by a double power-law where the large-scale ($\gtrsim 1 - 2 h^{-1} \text{Mpc}$) slope is equal to that of the conventional single power-law, i.e. $\gamma \sim 1.8$.
- The form of the angular correlation functions at large scales are consistent with the expectation of the linear perturbation theory in the flat standard ΛCDM Universe.
- The LRG linear bias is high, $b_g \sim 2.0$, as expected for massive luminous early-type galaxies and the clustering strength is found to be strongly linked to the sample intrinsic brightness.
- The clustering evolution at intermediate scales ($1 < r < 20 h^{-1} \text{Mpc}$) is remarkably slow and may be approximately explained by a long-lived model or even a no-evolution model. The long-lived model may be in line with the observed passive evolution of the LRG luminosity function, consistent with a constant comoving LRG space density in this redshift range. This latter conclusion would also apply in the case if the no-evolution (comoving) model were found to fit better but in this case the observations may require a significantly higher bias.

- Using the LRG biases, we are able to determine that the typical mass of dark matter haloes (M_{DMH}) occupied by the LRGs is $> 10^{13} h^{-1} M_\odot$. Using Lacey & Cole (1993) framework, our $M_{\text{DMH}}(z)$ measurements are well fitted by the model where halo mass is grown via merging of progenitors with masses of $\sim 1.4 \times 10^{13} h^{-1} M_\odot$ and $\sim 2.3 \times 10^{13} h^{-1} M_\odot$ from $z = 1$, for haloes that typically host $L \geq 2L^*$ and $\geq 3L^*$ galaxy, respectively. We found that these dark matter haloes have tripled their masses over the last half of cosmic time whereas it has been claimed that the LRG stellar masses have grown by less than 50 per cent (Cool et al. 2008).

- At small scales ($r < 1 h^{-1} \text{Mpc}$) the clustering evolution appears faster at fixed luminosity and the clustering increases towards lower redshift, consistent with a virialised clustering or even the linear theory prediction. These observational results are again consistent with those found in smaller 3-D redshift surveys, although our stable clustering model shows much slower evolution than the passive HOD model rejected by Wake et al. (2008). Since our virialised model assumes a constant comoving LRG space density, a combination of this stable clustering model at small scales and the long-lived model at intermediate scales could be consistent with the idea that merging of LRGs may not change the LRG space density significantly out to $z \approx 0.7$. It will then be interesting to see if a HOD prescription can be found in the context of the ΛCDM model that might naturally explain stable small-scale galaxy clustering with only limited galaxy merging.

- We observed a hint of the BAO peak in the combined results at a level consistent with the BAO detected by Eisenstein et al. (2005) but with somewhat too high an amplitude for the linear ΛCDM expectation.

- The excess signal in the our $w(\theta)$ relative to the standard ΛCDM model appears to be in good agreement with the C_l power excess at low l observed by other authors who used photo-z LRG samples at $z \approx 0.5$.

- If this power excess is interpreted as an artefact then the agreement with Eisenstein et al. (2005) is in fact accidental and would imply that our result is too much dominated by systematics to detect the acoustic peak.

- Further improvement could be achieved with smaller photo-z error, probably via Neural Network route but a sample of a few thousands $z \sim 0.7$ LRGs would be needed in order to obtain the required photo-z accuracy, given the already narrow redshift distribution of our sample in this analysis.

- The photo-z accuracy needed to robustly detect the acoustic peak in the angular correlation function of the LRGs at $z \approx 0.7$ is $\sigma_z \approx 0.03$ which may be the best the angular correlation functions can do. This limit should be achievable with the future wide-field imaging survey such as the Pan-STARRS 3π survey.

ACKNOWLEDGEMENTS

US acknowledges financial support from the Institute for the Promotion of Teaching Science and Technology (IPST) of The Royal Thai Government. We thank Michael J. I. Brown for useful comments. We also thank all the present and for-

mer staff of the Anglo-Australian Observatory for their work in building and operating the 2dF and AAOmega facility.

Funding for the SDSS and SDSS-II has been provided by the Alfred P. Sloan Foundation, the Participating Institutions, the National Science Foundation, the U.S. Department of Energy, the National Aeronautics and Space Administration, the Japanese Monbukagakusho, the Max Planck Society, and the Higher Education Funding Council for England. The SDSS Web Site is <http://www.sdss.org/>.

The SDSS is managed by the Astrophysical Research Consortium for the Participating Institutions. The Participating Institutions are the American Museum of Natural History, Astrophysical Institute Potsdam, University of Basel, Cambridge University, Case Western Reserve University, University of Chicago, Drexel University, Fermilab, the Institute for Advanced Study, the Japan Participation Group, Johns Hopkins University, the Joint Institute for Nuclear Astrophysics, the Kavli Institute for Particle Astrophysics and Cosmology, the Korean Scientist Group, the Chinese Academy of Sciences (LAMOST), Los Alamos National Laboratory, the Max-Planck-Institute for Astronomy (MPIA), the Max-Planck-Institute for Astrophysics (MPA), New Mexico State University, Ohio State University, University of Pittsburgh, University of Portsmouth, Princeton University, the United States Naval Observatory, and the University of Washington.

REFERENCES

Abdalla F. B., Banerji M., Lahav O., Rashkov V., 2008, ArXiv e-prints

Adelman-McCarthy J. K., et al. 2006, ApJS, 162, 38

Adelman-McCarthy J. K., et al. 2007, ApJS

Angulo R. E., Baugh C. M., Frenk C. S., Lacey C. G., 2008, MNRAS, 383, 755

Banerji M., Abdalla F. B., Lahav O., Lin H., 2008, MNRAS, 386, 1219

Baugh C. M., Efstathiou G., 1993, MNRAS, 265, 145

Benson A. J., Frenk C. S., Baugh C. M., Cole S., Lacey C. G., 2001, MNRAS, 327, 1041

Blake C., Collister A., Bridle S., Lahav O., 2007, MNRAS, 374, 1527

Blake C., Collister A., Lahav O., 2008, MNRAS, 385, 1257

Blake C., Glazebrook K., 2003, ApJ, 594, 665

Bruzual G., Charlot S., 2003, MNRAS, 344, 1000

Cai Y.-C., Angulo R. E., Baugh C. M., Cole S., Frenk C. S., Jenkins A., 2009, MNRAS, 395, 1185

Cannon R., et al. 2006, MNRAS, 372, 425

Carroll S. M., Press W. H., Turner E. L., 1992, ARA&A, 30, 499

Chambers K. C., 2009, in Bulletin of the American Astronomical Society Vol. 41 of Bulletin of the American Astronomical Society, Pan-STARRS Telescope #1 Status and Science Mission. pp 270–+

Cole S., et al. 2005, MNRAS, 362, 505

Colless M., et al. 2001, MNRAS, 328, 1039

Collister A., et al. 2007, MNRAS, 375, 68

Cool R. J., Eisenstein D. J., Fan X., Fukugita M., Jiang L., Maraston C., Meiksin A., Schneider D. P., Wake D. A., 2008, ApJ, 682, 919

Cooray A., Sheth R., 2002, Phys. Rep., 372, 1

Croom S. M., Boyle B. J., Shanks T., Smith R. J., Miller L., Outram P. J., Loaring N. S., Hoyle F., da Ångela J., 2005, MNRAS, 356, 415

da Ångela J., Shanks T., Croom S. M., Weilbacher P., Brunner R. J., Couch W. J., Miller L., Myers A. D., Nichol R. C., Pimbblet K. A., de Propris R., Richards G. T., Ross N. P., Schneider D. P., Wake D., 2008, MNRAS, 383, 565

Eisenstein D. J., et al. 2001, AJ, 122, 2267

Eisenstein D. J., et al. 2005, ApJ, 633, 560

Eisenstein D. J., Hu W., 1998, ApJ, 496, 605

Fry J. N., 1996, ApJ, 461, L65+

Fukugita M., Ichikawa T., Gunn J. E., Doi M., Shimasaku K., Schneider D. P., 1996, AJ, 111, 1748

Gladders M. D., Yee H. K. C., 2000, AJ, 120, 2148

Glazebrook K., et al. 2007, in Metcalfe N., Shanks T., eds, Cosmic Frontiers Vol. 379 of Astronomical Society of the Pacific Conference Series, The WiggleZ Project: AAOmega and Dark Energy. pp 72–+

Groth E. J., Peebles P. J. E., 1977, ApJ, 217, 385

Hamilton A. J. S., 1993, ApJ, 417, 19

Hamilton A. J. S., Kumar P., Lu E., Matthews A., 1991, ApJ, 374, L1

Hawkins E., et al. 2003, MNRAS, 346, 78

Kaiser N., 1987, MNRAS, 227, 1

Lacey C., Cole S., 1993, MNRAS, 262, 627

Landy S. D., Szalay A. S., 1993, ApJ, 412, 64

Lawrence A., et al. 2007, MNRAS, 379, 1599

Lewis A., Challinor A., Lasenby A., 2000, Astrophys. J., 538, 473

Limber D. N., 1953, ApJ, 117, 134

Lucy L. B., 1974, AJ, 79, 745

Lupton R., Gunn J. E., Ivezić Z., Knapp G. R., Kent S., 2001, in Harnden Jr. F. R., Primini F. A., Payne H. E., eds, Astronomical Data Analysis Software and Systems X Vol. 238 of Astronomical Society of the Pacific Conference Series, The SDSS Imaging Pipelines. pp 269–+

Martínez V. J., Saar E., 2002, Statistics of the Galaxy Distribution. Statistics of the Galaxy Distribution, Published by Chapman & Hall/CRC, Boca Raton, ISBN: 1584880848

McDonald P., Eisenstein D. J., 2007, Phys. Rev. D, 76, 063009

Mo H. J., White S. D. M., 1996, MNRAS, 282, 347

Moore A. W., Connolly A. J., Genovese C., Gray A., Grone L., Kanidoris N. I., Nichol R. C., Schneider J., Szalay A. S., Szapudi I., Wasserman L., 2001, in Banday A. J., Zaroubi S., Bartelmann M., eds, Mining the Sky Fast Algorithms and Efficient Statistics: N-Point Correlation Functions. pp 71–+

Navarro J. F., Frenk C. S., White S. D. M., 1997, ApJ, 490, 493

Norberg P., et al. 2002, MNRAS, 332, 827

Padmanabhan N., et al. 2007, MNRAS, 378, 852

Padmanabhan N., et al. 2008, ApJ, 674, 1217

Parkinson D., Blake C., Kunz M., Bassett B. A., Nichol R. C., Glazebrook K., 2007, MNRAS, 377, 185

Peacock J. A., Dodds S. J., 1996, MNRAS, 280, L19

Peebles P. J. E., 1980, The large-scale structure of the universe. Princeton University Press

Peebles P. J. E., 1984, ApJ, 284, 439

Percival W. J., Cole S., Eisenstein D. J., Nichol R. C., Peacock J. A., Pope A. C., Szalay A. S., 2007, MNRAS,

381, 1053
 Petrosian V., 1976, *ApJ*, 209, L1
 Phillipps S., Fong R., Fall R. S. E. S. M., MacGillivray H. T., 1978, *MNRAS*, 182, 673
 Phleps S., Peacock J. A., Meisenheimer K., Wolf C., 2006, *A&A*, 457, 145
 Ratcliffe A., Shanks T., Parker Q. A., Fong R., 1998, *MNRAS*, 296, 173
 Ross N. P., et al. 2007, *MNRAS*, 381, 573
 Ross N. P., Shanks T., Cannon R. D., Wake D. A., Sharp R. G., Croom S. M., Peacock J. A., 2008, *MNRAS*, 387, 1323
 Salpeter E. E., 1955, *ApJ*, 121, 161
 Sawangwit U., Shanks T., Cannon R. D., Croom S. M., Ross N. P., Wake D. A., 2009, arXiv:0911.1352
 Schlegel D. J., Finkbeiner D. P., Davis M., 1998, *ApJ*, 500, 525
 Scoville N., et al. 2007, *ApJS*, 172, 1
 Scranton R., et al. 2002, *ApJ*, 579, 48
 Seo H.-J., Eisenstein D. J., 2003, *ApJ*, 598, 720
 Shanks T., et al. 2007, in preps.
 Shanks T., Bean A. J., Ellis R. S., Fong R., Efstathiou G., Peterson B. A., 1983, *ApJ*, 274, 529
 Shanks T., Sutton D. H., Fong R., Metcalfe N., 1989, *MNRAS*, 237, 589
 Sheth R. K., Mo H. J., Tormen G., 2001, *MNRAS*, 323, 1
 Simon P., 2007, *A&A*, 473, 711
 Simpson F., Peacock J. A., Simon P., 2009, *Phys. Rev. D*, 79, 063508
 Smith J. A., et al. 2002, *AJ*, 123, 2121
 Smith R. E., Peacock J. A., Jenkins A., White S. D. M., Frenk C. S., Pearce F. R., Thomas P. A., Efstathiou G., Couchman H. M. P., 2003, *MNRAS*, 341, 1311
 Tegmark M., et al. 2006, *Phys. Rev. D*, 74, 123507
 Tinker J. L., Weinberg D. H., Zheng Z., Zehavi I., 2005, *ApJ*, 631, 41
 Wake D. A., et al. 2006, *MNRAS*, 372, 537
 Wake D. A., et al. 2008, *MNRAS*, 387, 1045
 White M., Zheng Z., Brown M. J. I., Dey A., Jannuzi B. T., 2007, *ApJ*, 655, L69
 Wolf C., Dye S., Kleinheinrich M., Meisenheimer K., Rix H.-W., Wisotzki L., 2001, *A&A*, 377, 442
 Yoo J., Fitzpatrick A. L., Zaldarriaga M., 2009, *Phys. Rev. D*, 80, 083514
 York D. G., et al. 2000, *AJ*, 120, 1579
 Zehavi I., et al. 2005a, *ApJ*, 621, 22
 Zehavi I., et al. 2005b, *ApJ*, 630, 1
 Zheng Z., Coil A. L., Zehavi I., 2007, *ApJ*, 667, 760